Medical Image Segmentation by Transferring Ground Truth Segmentation

By

Aseem Vyas

A thesis submitted to
The Faculty of Graduate Studies and Research
In partial fulfillment of
The degree requirements of
Master of Applied Science

School of Electrical Engineering and Computer science
Faculty of Engineering

Department of Electrical and Computer Engineering
University of Ottawa
Ottawa, Ontario, Canada
May 2015

The undersigned recommends to
the Faculty of Graduate Studies and Research
acceptance of the thesis

Medical image segmentation by transferring ground truth segmentation

Submitted by **Aseem Vyas**
In partial fulfillment of the requirements for the degree of
Master of Applied Science

_____

WonSook Lee, Thesis Supervisor

2015

Abstract

The segmentation of medical images is a difficult task due to the inhomogeneous intensity variations that occurs during digital image acquisition, the complicated shape of the object, and the medical expert's lack of semantic knowledge. Automated segmentation algorithms work well for some medical images, but no algorithm has been general enough to work for all medical images. In practice, most of the time the segmentation results are corrected by the experts before the actual use.

In this work, we are motivated to determine how to make use of manually segmented data in automatic segmentation. The key idea is to transfer the ground truth segmentation from the database of train images to a given test image. The ground truth segmentation of MR images is done by experts.

The process includes a hierarchical image decomposition approach that performs the shape matching of test images at several levels, starting with the image as a whole (i.e. level 0) and then going through a pyramid decomposition (i.e. level 1, level 2, etc.) with the database of the train images and the given test image. The goal of pyramid decomposition is to find the section of the training image that best matches a section of the test image of a different level. After that, a re-composition approach is taken to place the best matched sections of the training image to the original test image space. Finally, the ground truth segmentation is transferred from the best training images to their corresponding location in the test image.

We have tested our method on a hip joint MR image database and the experiment shows successful results on level 0, level 1 and level 2 re-compositions. Results improve with deeper level decompositions, which supports our hypotheses.

Acknowledgements

I wish to express my deepest gratitude to Prof. WonSook Lee, who give me this opportunity to do my research. I would not have been able to successfully complete my work without her guidance throughout the process.

I would like to thank my colleagues at the computer graphics lab, especially Mehdi Moghadas, Sadaf Arezoomand and Alberto Chavez, who guided me in my research work.

I would like to appreciate The Ottawa Hospital, especially Dr. Paul Beaulé and Dr. Kawan Rakhra for providing MRI images. The thesis has been supported by NSERC CHRP project titled by “Detection and simulation of femoroacetabular impingement”.

I would also like to thank my family and friends for their financial and moral support.

Table of Contents

List of Tables

List of Figures

List of Abbreviations

CP	Control Point
CT	Computed Tomography
FAI	FemoroAcetabular Impingement
FCM	Fuzzy C-Mean
MRI	Magnetic Resonance Imaging
SIFT	Scale Invariant Feature Transform

Chapter 1 : Introduction

1.1 Motivation

The hip joint is a major weight bearing joint. It consists of the ball shaped femur and acetabulum, which act as a socket. An abnormality in the shape of the femur head or of the acetabulum can cause Femoroacetabular impingement (FAI) [2].To study FAI, medical experts have to extract the boundaries of the femur and acetabulum in the medical images of the pelvic region. The extracted boundaries are used to understand the abnormality of shape in the hip joint structure. This segmentation is done manually by medical experts [1]. The segmentation of the hip joint structure is very time consuming, which is why an automated algorithm has been developed to segment the medical images.

Many different techniques are used for medical image segmentation. Some methods use the pixel attributes to make a clear distinction between the objects present in the image. Some of the popular methods that are based on pixel attributes are region growing, region merging, K-mean clustering, fuzzy clustering and other threshold based methods [4] [7] [34] [35]. In the region based methods, the pixels with similar intensity values, based on the similarity criteria, are grouped together as a region. These region based methods use a bottom-up technique to segment the object of interest [7]. Similarly, in the clustering methods, the pixels are clustered together to be placed into one of the

classes. The clustering method does not require the training phase; the algorithm trains itself from the available data. They classify the pixels into one of the classes, based on the similarity criteria [34]. The threshold techniques separate the pixels into binary regions based on the threshold criteria. The pixels below the threshold are considered part of one region, and those above it part of another region [4] [55]. These methods are easy to implement, but their major disadvantage is that they segment too much.

A model based segmentation approach involves prior knowledge about the shape of the object of interest. The previous model is used for the segmentation of the new image, while the snake and level set method uses energy minimization techniques to deform the model for image segmentation [12][18]. Another way to segment images based on prior knowledge is statistical shape based segmentation. The model is created from the training set of images, which contains a similar object. The method is based on the point distribution model, which creates a model that will execute the algorithm on a new image. The active shape and appearance models are statistical shape based approaches [4][58]. A limited amount of data to be used for the execution of the algorithm leads to poor results.

The above mentioned algorithms are only based on pixel attributes; they describe the shape of the object by checking the intensity variation in the image. Humans are better than computer algorithms at recognizing shapes, since they can extract the boundaries without knowing the intensity of pixels [1]. As medical experts still correct the segmentation obtained from computer algorithms, we have developed a novel technique to transfer the expert's segmentation to the new un-segmented image.

Our method is based on the pyramid decomposition, in order to match the test images to the database of MR images, which are manually segmented by experts. We match the test images with database images in order to find the best matched training image parts for each of the decomposed test image parts. The re-composition process is used to represent the test image using the mosaic of the best training image parts. Finally, the expert's segmentation from the best training image parts is transferred to the corresponding location in the original test image, to get the segmentation of the test image.

1.2 System Overview

The system is comprised of two phases: the first is the pyramid decomposition and the second is the re-composition. The overall process is shown in Figure 1, and the details of each step are as follows:

- Phase 1 (Pyramid decomposition): This phase consists of the preprocessing of the training image database and test image to conduct the shape matching of the test image over the training images. The test image is matched over the database of the training image and may be decomposed up to two levels in order to find a match.
- Phase 2 (Re-composition): This stage provides the best training image parts for each of the corresponding test image parts. The ground truth segmentation is transferred from the best matched training image part of the corresponding test image's original space.

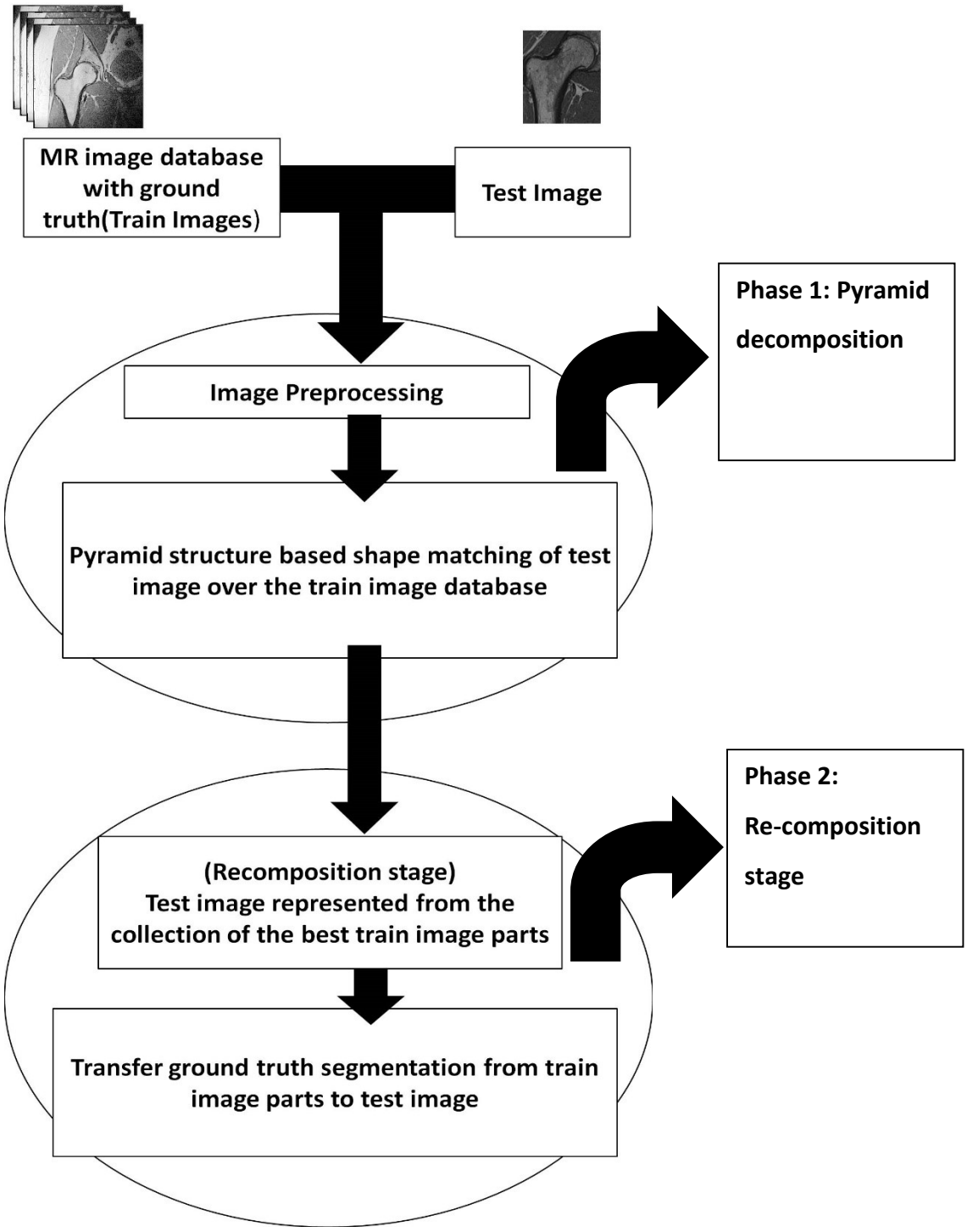

Figure 1: Algorithm Workflow

1.3 Thesis Overview

The following is a description of each of the chapters in the thesis:

- Chapter 2: We discuss the hip joint structure as well as the FAI problem and its diagnosis. We also cover medical imaging techniques such as the MRI, and explain the current methods being used in the field of image segmentation and image registration.
- Chapter 3: We describe the methodology of the algorithm.
- Chapter 4: The experimental details and results are discussed.
- Chapter 5: We conclude our work and propose future direction of the research.

Chapter 2 : Background

2.1 Hip-Joint Structure

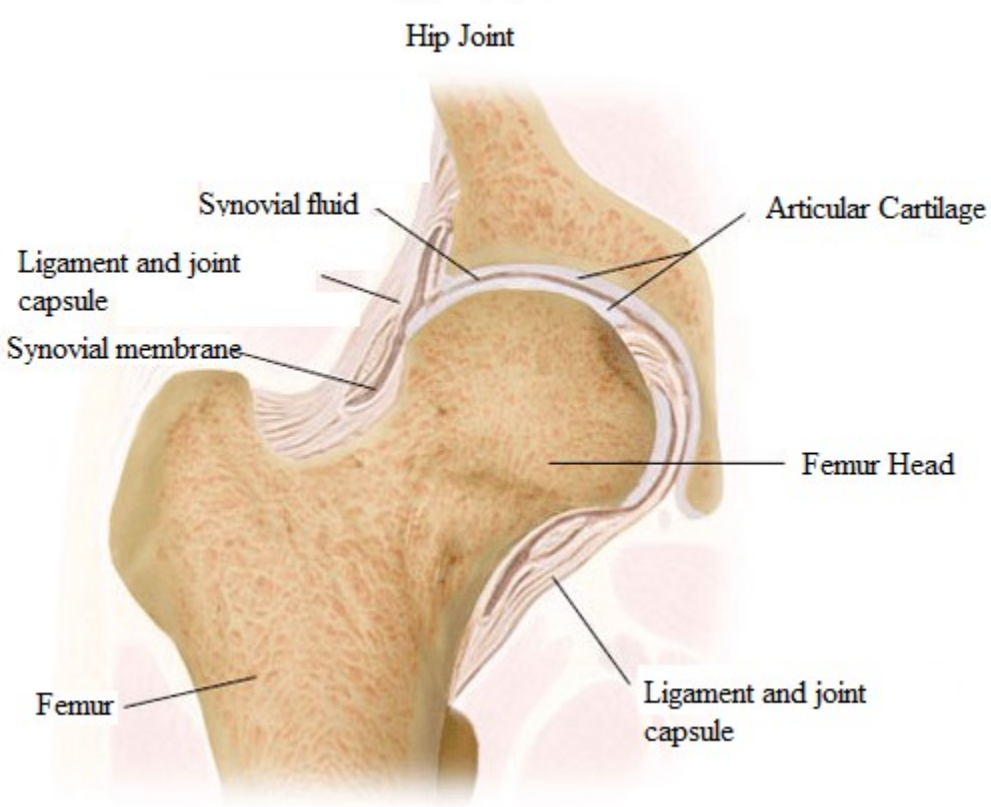

Figure 2: Hip-Joint Structure [22]

The hip joint consists of the femur head and the acetabulum; the femur head is ball shaped and the acetabulum is a socket, as shown in Figure 2 which is why it is called a

ball and socket joint. The hip joint is one of the major weight bearing joints in the human body. The femur head and acetabulum are covered with a soft cushion called articular cartilage. The cartilage is responsible for the smooth movement of the femur head and the acetabulum. The articular cartilage is kept slippery with synovial fluid and acts as a shock absorber; it protects the femur head and the acetabulum. The synovial fluid keeps the joint lubricated, which allows us to flex our muscles under great stress [23].

2.1.1 Femur

The femur, the strongest bone in the body, bears the whole weight of the body during activities such as walking and running. As shown in Figure 3, the femur is an elongated bone, divided into three parts viz. the upper extremity, the lower extremity, and the body [24].

The upper extremity consists of the femur head, a neck, and a greater and lesser trochanter. The head is part of the hip joint; it is globular and more hemispherical in shape, directed upward and medial ward. It is also smooth and covered with cartilage. The neck is the link between the body and the femur head. The shape of the neck is cylindrical and forms a wide angle opening with the head directed towards the middle. This angle of projection gives the range of motion of the hip joint. The greater and lesser trochanter act as levers for the muscles that rotate the thighs on the axis. The greater trochanter is located at the junction of the neck and the upper part of the body and has a lateral and backward direction. The lesser trochanter is conical in shape and projects from the lower back part of the neck [24].

The body of the bone is approximately cylindrical in shape and is broader above the center and flattened before the bottom of the backward. Its shape brings the knees closer to the center of gravity and therefore creates stability. The lower extremity is broader than the upper extremity and is connected to the knee. The shape of the lower extremity is that of a cuboid [25].

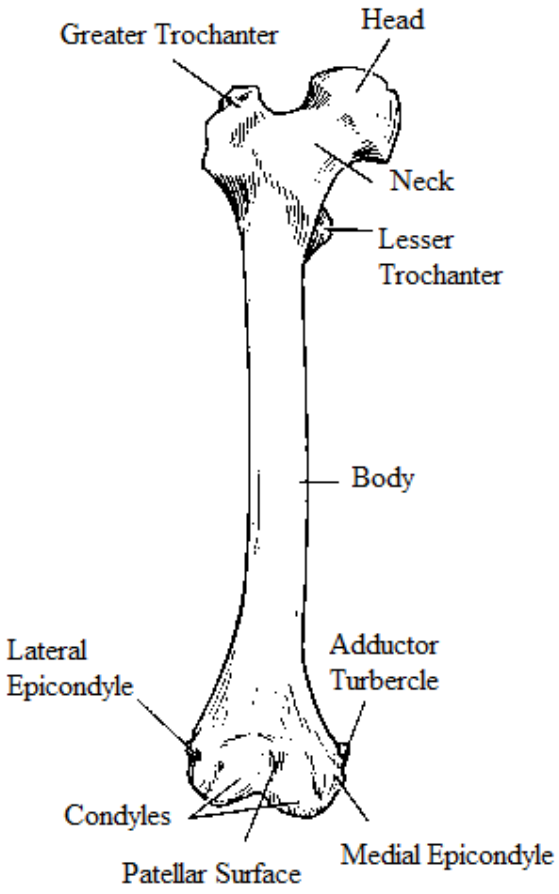

Figure 3: Femur Anatomy [71]

2.1.2 Acetabulum

The acetabulum is the curved surface of the pelvic region. It acts as a socket for the hip joint structure and allows a certain degree of freedom to the femur head to provide a set range of motion. The acetabulum is made up of three bones: ilium, ischism and pubis, as shown in the Figure 4. The ischism is approximately two fifths of the total structure, while the upper boundary formed by the ilium is less than two fifths[26] . The rest of the structure consists of the pubis bone. The acetabulum is covered with articular cartilage, which is lubricated by the synovial fluid to provide a frictionless movement of the femur head in the acetabulum.

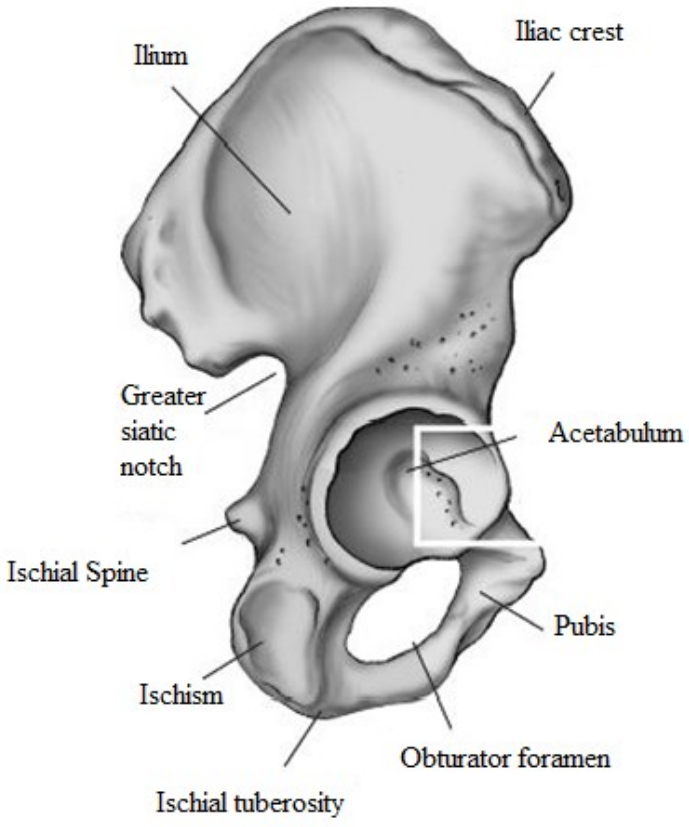

Figure 4: Acetabulum anatomy [72]

2.2 FemoroAcetabular Impingement (FAI)

As mentioned above, the hip joint is considered the ball and socket joint. The ball shaped femur head rotates in the acetabulum, which acts as a socket. An abnormality in the shape of the hip joint affects the range of motion and results in pain, mostly in the groin area. It is mostly young adults and athletes that suffer from FAI, a condition that causes chronic pain and decreases the range of motion of the hip joint. The patients have problems with positions that require hip flexion, for instance bending, or any flexion exercise and, in the worst cases, sitting [20][2]. FAI is also called pre osteoarthritis due to the constant friction between the femur head and the acetabulum; it may damage the articular cartilage, which is the cause of osteoarthritis.

We can classify FAI into three types: cam type impingement, pincer type impingement, and mixed type impingement, as shown in Figure 5. Cam-type impingement is caused by changes in the shape of the femur head. When the femur head isn't round, it cannot move properly in the acetabulum. The improper movement results in a shearing force on the labrum and on the articular cartilage. This type of impingement is more frequent in men. An abnormality in the shape of the acetabulum gives rise to pincer type impingement. The over-coverage of the femur head by the acetabulum leads to the contact of the labrum with the femur neck, which is just below the femur head. This impingement is common in middle aged women. The third is a mixed type; a combination of both cam and pincer type impingements [20].

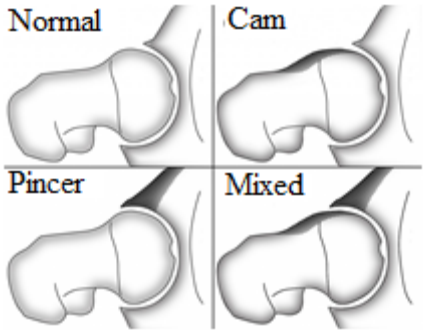

Figure 5: Different type of FAI [21]

2.2.1 Diagnosis of FAI

The repetitive impingement between the femur head-neck junction and labrum is the cause of pain in the hip joint. First, the pain is infrequent but activities that require the involvement of forceful flexion and internal rotation cause severe pain around the groin area. The physician tries to predict the type of impingement by checking the internal rotation of flexion and the adducted hip. There are two types of tests that can be done to determine which type it is.

First, the impingement test in which the physician adducts the hip and internally rotates it while it is flexed at 90^0. The abnormal shape of the hip joint puts the shearing force on the labrum and creates chronic pain in the groin [24]. The pain is the sign of impingement.

Second, imaging techniques are used to get a clear view of the abnormality in shape of the femur head or of the acetabulum. The X-ray technique produces the two dimensional view of the pelvic region and can show an abnormality in the shape of the bone, especially the femur head. The MRI shows the three dimensional view of the hip

joint structure and can show the damaged labrum, however it does not provide information about the surface of the hip joint. CT images are capable of showing the accurate shape of the bone and of an abnormality of the bone. CT imaging is good for arthroscopic surgery and would be helpful to reshape the bone[24] .

2.2.2 Treatment of FAI

The evaluation of FAI with imaging techniques provides an indication of the type of treatment needed for the patient. The treatment of FAI is possible in two ways, the first is non-surgical and the other is surgical.

The non-surgical treatment involves the physical evaluation of the joint structure to check the strength of the muscles of the hip and of the knee. The gait analysis is also conducted to check the walking pattern of the patient. All of the characteristics and factors observed lead to the creation of an activity program for the patient. The goal of the patient's physical activity program is to change the posture and increase the strength of the muscles, therefore restoring normal movement in the hip joint [17][19].

On the other hand, the patient may choose to undergo surgical treatment if the pain persists after the non-surgical treatment. The surgical treatment is conducted in three ways. The first is fully open surgery, which involves the dislocation of the femur head from the socket in order to correct and reshape it. The second is arthroscopic surgery, it does not require the dislocation of the femur head from the acetabulum. The third is osteotomy, which is done for the pincer type impingement. If the cartilage is damaged, then a total hip joint replacement may be needed [19].

2.3 Magnetic Resonance Imaging (MRI)

Magnetic resonance imaging is an imaging technique that uses magnetic fields and radio waves to take images of the organs and tissues inside the body. MRI techniques provide different information about body organs than do the other imaging technologies like X-ray, Computed tomography (CT) or Ultrasound. MRI is used to obtain a clear view of the soft tissue of the organs. It is used for the examination of brain, knee, joints, blood vessel, and heart values. Contrast is used to indicate certain organs more clearly than the rest [27].

The human body consists of 70% water, which is composed of hydrogen and oxygen atoms. MRI uses the hydrogen atom to take a picture of the organs. The moving proton creates a magnetic field around it, and the external magnetic field aligns the human body's protons. Due to external magnetic field, the external protons start rotating about the axis of the external magnetic field. Very few protons are aligned with the external magnetic field, so they have less energy and a more stable state. The radio frequency (RF) pulse is applied to the protons; it absorbs energy and jumps to a higher energy state. The RF pulse tunes the protons until they are in phase. The higher energy protons reach a normal state and emit a radio frequency signal. The signal received is the measure of the radio wave with time [28][29].

2.4 Region Based Segmentation

Region based image segmentation is the partition of the image into a number of regions. The common method is to compare the neighboring pixels with another pixel, and if the similarity criteria are satisfied, then assign that pixel into the region. The similarity

criteria can be the intensity value, variance, color, texture or many more. Region based segmentation can be classified into three categories: region growing, region merging and splitting, and hybrid region based segmentation [10] [14] .

Region growing is the simplest region based segmentation. The region growing algorithm starts with a seed pixel, which is compared to the neighboring pixels based on the similarity criteria. It is an iterative method that adds pixels to a certain region, according to the similarity criteria. The choice of the seed point is crucial for the final segmentation; the selection of the seed point may be manual or automatic. It can be obtained through various methods such as the Harris corner detection theory or the cost minimization problem, as in [30][31]. In [32], we see the segmentation of the abdominal images of the liver is done by the region growing algorithm; the selection of the seed point is done manually. It is the simplest form of region based segmentation, but it can sometimes be affected by the noise, which may lead to an over segmentation.

The region based split and merge algorithm can be represented by the pyramidal structure. The algorithms are divided into two stages, the first of which is splitting the image into a number of regions. To begin, the whole image is considered as one region. The homogeneity criteria are then verified and identified as true or false. If false, the whole region is divided into four regions; the process is repeated until we find a homogeneous region. The merge stage consists of merging the small regions that satisfy the homogeneity criteria [7] [10].

2.5 Clustering Based Segmentation

Clustering is an unsupervised task that does not have a learning stage; the clustering algorithm learns from the available data. The clustering algorithms classify the data into a number of clusters depending on the similarity criteria. The clustering method can be divided into two categories: hard clustering and soft clustering.

K-mean clustering, a type of hard clustering, classifies the pixels into k clusters based on the similarity condition. The method randomly divides the image into k clusters with their respective centroid. The distance of each pixel from the center of the cluster is calculated, and according to that distance, each pixel is grouped into one of the k clusters. The mean of the clusters is measured iteratively until convergence. The K-mean cluster can be adaptive, and the initial selection of the k cluster is based on the input data[33] [34].

The second type of clustering is soft clustering, for example fuzzy c-mean (FCM) clustering. In fuzzy c-mean clustering, the pixel can be associated with more than one cluster. The pixels are classified into a cluster with their associated weight. The weight represents the degree to which the pixel is associated with the cluster [35] [36]. The FCM algorithm's goal is to minimize the objective function [43]. The fuzzy c mean algorithm is combined with other methods in order to obtain better segmentation. In [41], FCM and mutual information are used to get good segmentation. The threshold is decided by the FCM algorithm for the iterative process and by maximizing the mutual information provided by the optimal threshold. Medical image segmentation is a difficult task due to

noise and inhomogeneity in the pixels. The filter is incorporated with an FCM algorithm to remove noise and clustering errors that occur due to noise [42].

2.6 Threshold Based Segmentation

Threshold based segmentation is one of the most important methods for the discrimination of foreground and background pixels in an image. The threshold is selected to convert a grayscale image into a binary image. The pixels above the threshold are considered true values in the binary image, and the pixels below it are considered false. Threshold based segmentation provides important information about the shape and position of an object. It can be calculated with different techniques such as the means threshold, the Otsu technique, manually, p-tile and much more. The selection of the threshold values is very important for the segmentation.

Threshold based segmentation is used in conjunction with other techniques. For instance, the Otsu threshold and the morphological operation are combined to get the segmentation of the MR images, which are then further combined with the original MR images to obtain the resultant output, containing the background brain image [54]. The threshold methods are used with existing segmentation techniques such as FCM and the level set method to improve the accuracy of the segmentation according to its stability [55]. The threshold can be adaptive in nature; it changes dynamically over the images, for each pixel threshold can be calculated. As in [56], the optimal threshold for the segmentation of a gray scale image is measured by the auto adaptive threshold algorithm [59].

2.7 Graph Cut Segmentation

Graph cut segmentation is based on the graph representation of the image, which is segmented by the graph cut. The graph is denoted by G=<V, E>; V represents the vertices, E is the edge in the graph, and the vertex V consists of the nodes. The neighboring pixels are considered one kind of node and the other nodes are called terminal nodes; they have a source (s) and sink (t). Therefore, the s node represents the object in the image and the t node is the background. The edge of the graph is the connection of vertices; each graph consists of two types of edges. The neighboring pixels are connected by an n-link, and a t-link connects the terminal node with pixels. The non-negative weight is associated with the edges in the graph [37][38] and is considered a cost. The cut is made on some of the edges. The sum of all the weights is considered the total cost. The aim is the minimization of the cost for the maximum flow [39][47]. The graph cut segmentation is classified into two categories: the interactive graph cut and the prior knowledge based graph cut.

The interactive graph cut segmentation requires the user to select the object of interest in the image, after which the bounding box is selected for this object of interest. The object is considered as the foreground and the area outside the object of interest is the background [45]. In medical image segmentation, accuracy is top priority. Sometimes, the automatic graph cut is challenging due to intensity variation, noise, and many other factors. A small input from the user can change the ambiguous decision about the segmentation of the object of interest [40][45][46]. The interactive graph cut can therefore improve segmentation efficiency. The shape prior knowledge is incorporated

with the energy function of the graph cut segmentation to increase robustness. The shape information can be statistical shape knowledge or parametric shape prior, the energy function of the shape information is combined with the energy function of the graph cut algorithm.

2.8 Model Based Segmentation

The active contour is the spline energy minimization technique for image segmentation. This method consists of the external constraints and image forces that attract the spline toward image features such as edges, lines, and subjective contours. The deformable model is used to segment the object of interest. The total energy is the sum of the internal energy and of the image forces, which is minimized to match the deformable model to the images. We represent the position of the snake by . The total energy is defined as

$$E_{snake} = \int_0^1 E_{int}\ (v(s) + \ E_{image}\ \big(v(s)\big) + \ E_{con}\big(v(s)\big)ds.$$

Where E_{int} is the internal energy that makes the contour smoother, E_{image} is the image forces, E_{con} is the external constraint force. The internal energy function is the control continuity spline, which can be the represented by

$$E_{int} = (\alpha(s)|v_s\ (s)|^2 + \beta(s)|v_{ss}(s)|^2)/2$$

The equation is manipulated by the parameters; $\alpha(s)$ is the first order term, and creates the membrane. $\beta(s)$ is the second order term, and makes it act like a thin plate spline [12].

The image forces in the equation attract the model to the image's features. The image's features are the edges, lines, and termination. A weight is given to each of the

features and their sum represents the image force. The external forces are responsible for putting the snake near the decomposed minimum. There are other implementations of snakes, for instance the Gradient vector flow, Balloon snake, Diffusion snake, and Geometric active contour [13] [16].

The segmentation problem can be formulated into a mathematical problem [4]. In the medical image segmentation, many segmentation problems are solved by the partial differential equation. The level set method is based on the partial differential equation; the main idea is to represent the curve at the zero level set at the higher dimensional hyper surface. The curve evolves with speed in a normal direction to itself. The partial differential equation can be derived at any time. As the curve evolves, the algorithm converges at the boundary of the object, where the difference between the pixels is highest [18]. The disadvantage of the level set method is over segmentation. Since the stopping function is never zero at the edge, the algorithm exceeds the edge and results in over segmentation [4].

In [48], the level set methods used for the topological feature in the image and the level set provide shape information for the image, which is used for the fuzzy c mean algorithm, to get the final segmentation. The main drawback of the level set method is over segmentation; to overcome this problem, we need to incorporate prior shape information in the Chan-Vese model [49] [57].The statistical shape model approach uses the set of shapes for the analysis of statistical and geometrical properties in order to segment the object of interest [8] [9] [11]. The statistical shape model method is based on the point distribution model and is divided into two categories: the active shape model

and the active appearance model. In the active shape model, the model is constructed from the collection of landmarks from the set of the training shapes. The model is allowed to deform iteratively within the range of the training shapes, to fit with the object of interest in the image. On the other hand, the active appearance model uses both shapes and gray level information to segment the object of interest [58] [60].

2.9 Image Registration and Shape Matching

In the field of medical image processing, image registration plays an important role. Image registration is the process of alignment of one image (sensed image) over the other image (reference image). Image registration plays an important role in medical image analysis; it is useful for image analysis when images are acquired at different times (multi-temporal), different viewpoints (multi-view) and different sensors (multimodal) [69]. The image registration process consists of the four stages.

- Feature detection: The key points in the image such as edge, lines, blob and corners are detected [68]. The detection can be done manually or automatically. There are different techniques for the automatic feature detection, for instance the Harris corner detection, SIFT, the canny edge detector, and many more. These techniques are also called control points (CP).
- Feature matching: The features are detected from both the sensed and reference images and matching is done by measuring the distance between the features of the two images. The Hausdorff distance, the Euclidean distance, and the Chamfer distance are some of the distance metrics.

- Transformation model: The mapping function develops the relation between the sensed image and the reference image. The type and parameter are estimated to overlay the sensed image on the reference image. The transformation can be divided into two categories, the global model mapping function and the decomposed model mapping function. In global model mapping, all control points are estimated for the mapping function. On the other hand, decomposed model mapping considers the images as the composition of patches and depends on their location in the image.
- Image resampling and transformation: The sensed image is transformed according to the mapping function's estimation parameter. The transformation can be done in two ways, forward and backward. The non-integer coordinates in the image can be computed by interpolation [69].

2.10 Image Registration Methods

The image registration methods are classified into two broad categories, i.e. feature based image registration and intensity based image registration.

2.10.1 Feature Based Image Registration

In the field of medical image registration, the features of the sensed and reference images are called control points (lines, edges, points). The objective of image registration is to find the spatial relationship between the features of the sensed and reference images. The distance metric is used to evaluate the similarities between the features of the sensed and reference images. The Hausdorff distance, chamfer distance, or Euclidian distance can be incorporated as similarity metrics [6] [63]. In medical image registration, due to noise, it

is difficult to detect the various parts of an image. Rucklidge suggested the improved similarity metric to resolve this problem and properly detect the object in the image [3]. The partial Hausdorff distance is minimized to obtain the transformation of the model to match with the object in the image [61] [63] [65] [67]. The variation in the similarity metric (Hausdorff distance) like the mean Hausdorff distance and the LTS-Hausdorff distance are used for medical image registration [5] [15] [64].

The other method used to describe the shape is the image moment. The object is extracted and its respective properties are evaluated. Hu calculated the image moment and its properties such as area, centroid and orientation etc. [69]. The best feature of the image moment is that it is invariant to translation, scaling and rotation. The boundaries are detected from sensed and reference images and moments are evaluated for each of the other closed boundary region properties like the chain code representation of the shape of the object.

Lowe proposed a scale invariant feature transform (SIFT) algorithm that extracts the key points and computes its descriptor. SIFT is based on the decomposed features and helps find the extrema in the scale space, in order to evaluate the information about the position, scale and rotation [44]. The feature distance is measured by the Euclidean distance and improper matching is removed with the help of the RANSAC algorithm. As in [44], a coarse to fine strategy is used for better image registration; the learning process occurs in the coarse to fine approach by selecting and mixing a large number of features. Similarly, the template matching method is based on the decomposed sections and is used for the detection of human parts. The chamfer distance is used for the similarity

measurement, and global to hierarchical part matching is used to detect human parts more accurately [6] [62] [70].

2.10.2 Intensity Based Methods

The intensity based methods do not focus on the shape of the object, but rather work on the pixel intensity values in the image. The method combines both feature detection and matching, in one step. The template matching or correlation method is sometimes called the area based method. In the template matching method, the rectangular window of the sensed image or whole image is used for the correspondence estimation during the registration step. An example of an area based method is the cross correlation method [69]. The cross correlation is calculated within the window from the sensed image and reference image. The algorithm searches for the maximum correlation. The method deals with the direct pixel intensity value and not with shape information. The disadvantage of the cross correlation method is that a rectangular window is only suitable for the images that undergo translation, and has a high computational cost.

To avoid the high computational cost of the cross correlation method, the Fourier methods are used instead. The idea behind the Fourier method is to represent images in the frequency domain. Phase correlation is based on the Fourier shift property, and a shift in the spatial domain is equivalent to the phase difference in the frequency domain for both sensed and reference images. The phase correlation is the cross power spectrum of the sensed and reference images and finds the peaks in its inverse. The method is robust and has lower computational cost. The images have scale variation, and a log polar

transform is combined with a phase correlation algorithm for image registration. The log polar transform is known for its scale and rotation invariant properties [69].

Mutual information based image registration is one of the most popular techniques in the field of medical image registration. It is an area based method used for multimodal registration. Mutual information is based on an information theory; it shares the amount of information in random variables with other variables. Mutual information based registration is suitable for the multimodal registration [53] [66]. The strategy with resolution control from coarse to fine is applied to obtain fast image registration. As in [50], the image is partitioned through the quad tree or BSP algorithm and mutual information is used as a stopping criteria. The registration of the partition image is done through the Powell optimization. Mutual information based registration only involves the intensity value. As in [51], shape information is combined with mutual information to obtain coarse to refined medical image registration. Mutual information is used as a dissimilarity measure, as are the transformation parameters obtained from optimization algorithms such as graph cut [52]. Deformable registration algorithms like fluid, demon, and curvature based techniques are only for mono modality. The 2-class based algorithms for global mutual information is pursued by local piecewise refinement [53].

Chapter 3 : Methodology

The method used in this work is to represent a test image as a mosaic of a set of training images where the set is chosen to be best matching to the given test image. So we uses a pyramid decomposition of an image where each piece of the sub blocks are chosen using image matching. The shape on an image is considered as an image similarity criteria and we used Hausdorff distance of the test image with train images. Then a re-composition is processed to collect the best matching pieces of test images. The test image is represented based on a collection of the best train image sections. Then the ground truth segmentation information of the training images is transferred to the test image.

3.1 Hausdorff Distance

The Hausdorff distance is the metric used to measure the degree of mismatch between the shapes of two images. It is the max-min distance between two sets of points. To calculate the distance between two images, the boundaries (edge image) are extracted from both the test and train images. The edge image represents the set of points for the test and the train images. Given a test image A and a train image B, the Hausdorff distance is defined as:

$$H(A,B) = \max(h(A,B), h(B,A))$$

where

$$h(A,B) = \max_{a \in A} \min_{b \in B} \|a - b\|$$

The *h (A, B)* is the directed Hausdorff distance. It is defined by considering every point of *A*, calculating the distance from each point of *A* to the closest point of *B,* and identifying the maximum among them [3]. The Hausdorff distance is sensitive to noise and outliers; this can be corrected by using the partial Hausdorff distance. The directed partial Hausdorff distance is defined as:

$$h_k = K^{th}_{a \in A} \min_{b \in B} \|a - b\|$$

where denotes the *K*th ranked value among the measured distances. The distance between each point of A and the closest point of B is calculated. The points of B are then sorted according to their distances, and the *K*th value will indicate that the *K* of the model point of A is within the distance of d with some points of B.

The partial Hausdorff distance gives bad results with corrupted data; we therefore need a more robust measure to solve the problem of corrupted data. The least trimmed square (LTS-HD) Hausdorff distance is a more robust measure. It is defined by the linear combination of order statistics. LTS Hausdorff distance is defined as:

$$h_{LTS}(A,B) = \frac{1}{k} \sum_{i=0}^{k \in A} \min_{b \in B} \|a - b\| \, (i)$$

where *k* is *K=f.N* and N is the number of points in the chunk of A. The value of *f* is in the range of 0.1~0.9. We used LTS-HD as a similarity metric to detect the test image model in the database of train images. The Hausdorff distance is more robust and less sensitive

to occlusion compared to other shape matching metric like chamfer distance, Euclidean distance.

3.2 Simulated Annealing

The simulated annealing is a search algorithm that searches for the optimal solution in a given search space. As there are many solutions that exist in a search space, finding the optimal solution is a time consuming process. Simulated annealing is analogous to the annealing process of metal. The metal is heated to a high temperature in order to change its internal structure. At a high temperature, molecules are excited to a higher state and they can move freely. The metal is cooled down slowly to obtain the desired structure. The simulation of annealing process is done in a very similar way, with the heating process being controlled by the temperature variable. At a high temperature, the algorithm finds many solutions to choose from, but as it cools down, it has less options and the global optimum solution can be found [5] [15]. The major advantage of the simulated annealing optimization method is that it ignores the decomposed minima in hopes of finding the global minima.

The system tries to minimize the energy with a cooling process. To find the best solution in the search space, the algorithm updates the solution and compares it with the current solution, at each iteration. The algorithm accepts the solution if it lowers the objective function or the system energy, otherwise we can accept the solution based on certain conditions. The acceptance of the selected solution depends on the metropolis criterion [73].

The metropolis algorithm dictates the acceptance of the solution with a probability $\exp\left(-\frac{\Delta E}{K_B.T}\right)$ based on $E_j - E_i \geq 0$ where a current state i and energy E_i and an updated state j with the energy E_j are used. T is the temperature parameter and K_B is the Boltzmann's constant.

At a high temperature, the updated solution can be accepted, but this is difficult at a low temperature. The annealing process depends on the different parameters, namely the initial and final temperatures, and the cooling down algorithm. The initial temperature set the starting point for the algorithm and the final temperature is the temperature at which the algorithm will stop. The cooling down process is to the method used to decrease the temperature in order to find the optimal solution; a slower process results in a better solution.

3.3 Database of MR Images

The segmentation of an image can be done in three ways: 1) automatic 2) semi-automatic 3) manual [1]. The automatic segmentation is based on the intensity of the images. It can be done in one of two ways. First, pixels with similar intensity values are considered as a similar region, which is often called region based segmentation. Second, there is the division of an image into regions based on the dissimilarity of pixel intensity. One of the disadvantages of intensity based segmentation is over segmentation. The semi-automatic image segmentation involves the intervention of a human. The user defines the region of interest for the segmentation. The manual segmentation does not involve the use of any computer algorithms and is therefore very time consuming. However, humans are much

better than computers at recognizing shapes [1]. The computer based segmentation of medical images is not ideal, which is why it needs to be corrected by experts. In our system, we created a database of manually segmented MR images of hip joint structures, done by experts. It includes both MR images and manually segmented MR images. The manually segmented images are considered the ground truth images. The database contains 20 MR images of the hip joint structure. These images are defined as train images.

3.4 Image Pre-Processing

The Hausdorff distance calculation is based on the boundaries of the images. The canny edge detection algorithm is used for the boundary extraction. Note that the canny edge detection is not used for the purpose of segmentation of bone boundaries, but to provide the Hausdorff distance calculation that is for image similarity measurement based on shape. This algorithm is based on two variable parameters. First, the size of the Gaussian filter (σ), as its variation causes a change in the length of the edges. A smaller size leads to small edges, but it might cause noise, and a large size leads to longer edges. In our system, we used a large Gaussian filter (σ) for the boundary extraction. Second is the threshold parameter, which we calculated for the train images using the Otsu method. The Otsu method calculates the global threshold of the image. The threshold level is used in the canny detection algorithm to convert a grayscale image into a binary image. The given information about the size of the Gaussian filter provides the short or long edges in the binary image. The canny edge detector has better signal to noise ratio and low error rate compared to other edge detection methods such as Sobel, prewitt and Laplacian.

3.5 Geometrical Transformation

The geometric transformation is the process of mapping one point of the plane to another. The transformation involves a set of operations such as translation, rotation, shearing and scaling. The combination of translation and other linear transformations like scaling, shearing and rotation is called affine transformation. The affine transformation preserves the parallelism. A transformation that includes only translation and rotation is called a rigid transformation, as it preserves the angles between the lines. The points in the space and transformation can be expressed in the form of a matrix. The point can be expressed as a column vector or row vector. A point in the plane can expressed as $\begin{bmatrix} x \\ y \end{bmatrix}$ or$[x \quad y]$. The transformation matrix can be represented by by M=$\begin{bmatrix} a & b \\ c & d \end{bmatrix}$. The transformation of the point p will give a new point p', and the new point can be represented as $p' = \mathrm{M}p$.

- Scaling: This operation multiplies the point by the scalar in x and y directions.

$$p' = \begin{bmatrix} a & 0 \\ 0 & d \end{bmatrix} p$$

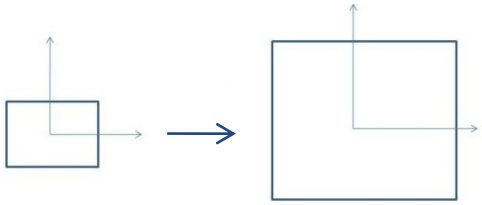

- Rotation: This operation rotates the point around the origin in a clockwise or anti-clockwise direction.

$$p' = \begin{bmatrix} \cos(\theta) & -\sin(\theta) \\ \sin(\theta) & \cos(\theta) \end{bmatrix} p$$

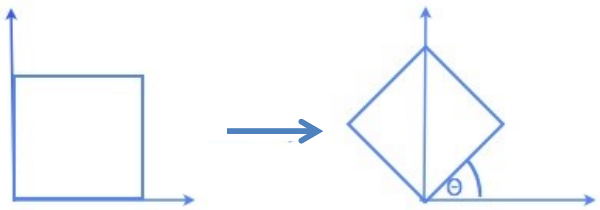

- Shearing: This operation deforms the point in either x direction or y direction.

$$p' = \begin{bmatrix} 0 & b \\ c & 0 \end{bmatrix} p$$

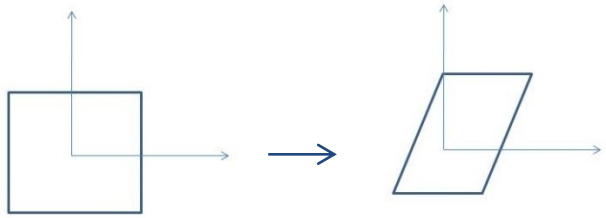

- Translation: This operation moves the points in a particular direction.

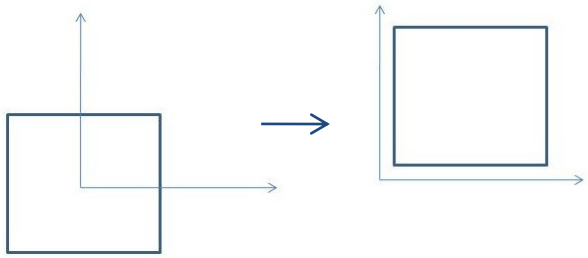

3.6 Pyramid Decomposition

Pyramid decomposition is the process used to decompose a test image into smaller parts to make it easier for it to be matched to a selected train image. As we can see in Figure 6, the hierarchy of the pyramid is represented by the levels in the pyramid structure. The levels of the algorithm are represented by L_i, i = 0, 1, 2, where the base level or level 0 is the global detection of the test image over a set of MR images (train images). The Hausdorff distance based shape matching algorithm is used for the detection of the test image over the train images. The shape matching algorithm uses the boundaries of the test image and train images, and the canny edge detector is used for the extraction of the image boundaries. Edge is not only feature for matching but other features like SIFT, Harris corner, Intensity can be used for image matching.

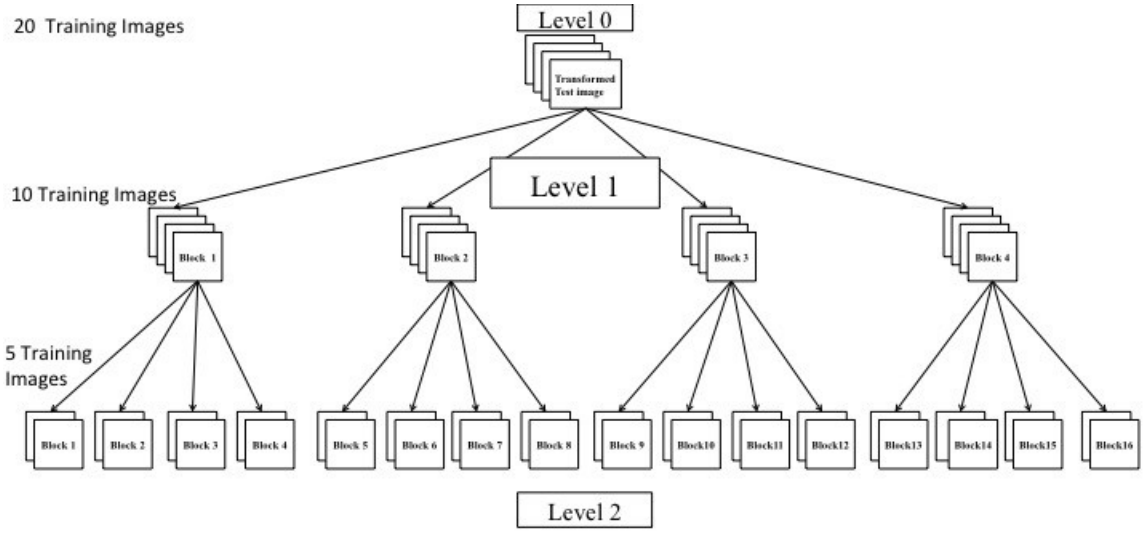

Figure 6: Pyramid decomposition

Given a test image *M* and train images IMG_1, IMG_2….IMG_n, the objective of shape matching is to obtain a transformation *T* to find similarity by the minimization of

Hausdorff distance as the similarity metric. The affine transformation maps the point in one plane to the other plane. The affine transformation parameters are scaling, rotation and translation. Let $p= (x_1, y_1)$ represent the point of the test image and (x_2, y_2) be the transformation point, then the transformation is defined as:

$$\begin{bmatrix} x_2 \\ y_2 \end{bmatrix} = \begin{bmatrix} \cos\theta & \sin\theta \\ -\sin\theta & \cos\theta \end{bmatrix} \begin{bmatrix} x_1 \\ y_1 \end{bmatrix}, \begin{bmatrix} x_2 \\ y_2 \end{bmatrix} = \begin{bmatrix} x_1 \\ y_1 \end{bmatrix} + \begin{bmatrix} t_x \\ t_y \end{bmatrix}, \begin{bmatrix} x_2 \\ y_2 \end{bmatrix} = \begin{bmatrix} S_x & 0 \\ 0 & S_y \end{bmatrix} \begin{bmatrix} x_1 \\ y_1 \end{bmatrix}.$$

where S_x and S_y are the scaling parameters in x and y directions. The translation parameters are t_x and t_y in x and y directions and, the rotation parameter, in either the clockwise or anticlockwise direction. The transformed point (x_2, y_2) is close to the points of the train image. The next task is to search for the best possible transformation, in the given search space, where the Hausdorff distance is minimized. Simulated annealing optimization is a search algorithm that searches for the best possible transformation of the test image, which is most similar to the train image. The test image is matched with all of the train images in the database. Each shape match provides the Hausdorff distance and affine transformation parameters. The train images are sorted in ascending order, based on the Hausdorff distance. Only half of the twenty train images are selected from the database for the next level. Each level and block of the test image is represented by *TestImage_i.j.k* where i is the level of the pyramid, j is the block of the level, and k is the image number of the training image of the block.

Test Image_i.j.k
i = Level of the pyramid
j = Block of the pyramid
k = Image number of the train images of the block

The train images are selected with their respective transformation parameters. Scaling and rotation is used for the test image transformation. Thus, the total number of transformed images is 10. Each of the transformed test images is decomposed into 4 parts using a cropping algorithm, as shown in Figure 6. Level 1 of the pyramid has 4 decomposed parts of each of the transformed test images of level 0. Each level has transformed test images, which is a decomposition of the preceding level. At each level, the decomposed parts are matched with the selected train images. The train image is again sorted in ascending order based on the Hausdorff distance obtained in the shape matching process of the decomposed parts. The transformed test parts at level 1 (L_1) have four blocks, each of which have 10 decompositions. For example, Test Image_1.1 has 10 images and each of them is matched with the selected train image. The train images are sorted according to the Hausdorff distance and every time the algorithm progresses to another level, half of the images of the previous level are taken. The images taken are the best images from that level for that block. For example, from the Test Image_1.1, images IMG_10, IMG_13, IMG_14, IMG_15, IMG_16 are selected for level 2 (i.e. for Test Image_2.1) shape matching.

Level 2 has 80 decomposed images. Each of the images of the blocks on level 1 is transformed and decomposed into four parts for level 2; each contains five best decompositions (images) from the previous level. At level 2 (L_2), the decomposed parts are matched with selected train images. For L_2, only rotation and translation are used as transformation parameters for local block registration, based on the Hausdorff distance. The train images for L_2 are sorted in ascending order based on their Hausdorff distance.

The train image with the lowest Hausdorff distance is selected, with its transformation, as the best training image for its corresponding test image of the block, at level 2. Finally, each of the blocks of level 2 are transformed and matched with their best train image. In the end, there are 16 local parts with their 16 best train images. We stop the decomposition of test image parts at level 2 for our experiment, but it can go to level 3, level 4, and so on depending on applications.

3.7 Re-Composition Phase

The re-composition approach aggregates all of the best parts of the train image, and represents the test image from this collection of best train image parts. As in the previous section, each of the decomposed images of the blocks at level 2 have their corresponding best match train image. For each of the decomposed images at L_2, the corresponding best matched train image is cropped to the same size as the decomposed image at L_2, i.e., the train image parts. The decomposed best matched images of L_2 are replaced by the corresponding train image parts. The best matched train image parts at L_2 are inversely transformed. As mentioned above, the transformation parameters obtained for the best matched train images, specific to each level, are inversed.

The inverse scaling parameters are $1/S_x$ and $1/S_y$ in x and y directions. The inverse rotation is a negative angle of rotation; if the decomposition parameter is clockwise, then the inverse rotation is anti-clockwise. The $-t_x$ and $-t_y$ are the inverse translations in x and y directions. As we climb up the pyramid, at every level, we merge the best train parts into one region and, as we can see in Figure 7, the final image is the mosaic of the best parts of the train image.

The test image is represented by the collection of the best parts of the train image. The database consists of the ground truth of these train images. The ground truth segmentation is transferred from the train image parts of the test image to their corresponding location. Finally, the segmentation of the test image is the collection of the ground truth segmentation of the train images.

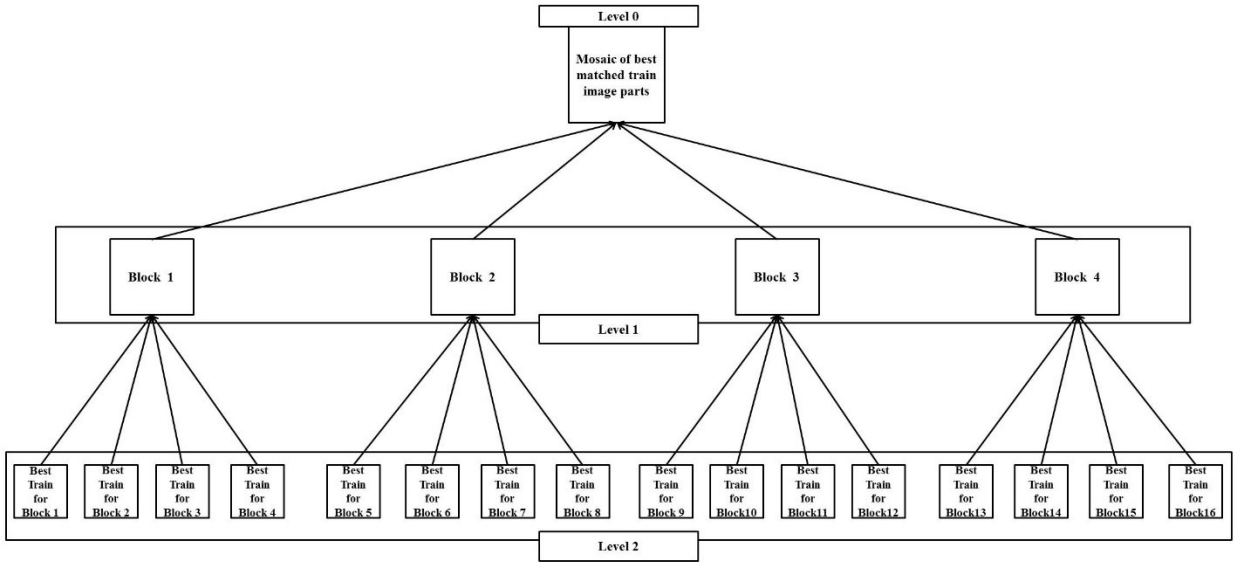

Figure 7: Re-composition of the best matched train parts

Chapter 4 : Experimental Results

In this chapter, we discuss the experiments that were conducted for the segmentation of the femur bone of the hip jointto . The results shown are those of the pyramid hierarchical order of global shape matching and decomposed image matching of the test image with the database of train images, and the re-composition of the best matched train image parts as well as the final segmentation with the transfer of the ground truth segmentation. The system is implemented in MATLAB 7.12.0.635 (2011a) at Intel core i7-2670 QM CPU@ 2.20 GHz. The system consists of a MATLAB global optimization toolbox for simulated annealing optimization and an image processing toolbox for the canny edge detector and affine transformation functions. We implemented the Hausdorff distance in the MATLAB.

4.1 Database of the MR Images and Test Image

The database of the MR images of the pelvis region shows the sagittal view of the femur bone of the hip joint. The database consists of 20 256x256 images. The test image size is 155x123 as it is cropped from the test MR image dataset. The database of MR images and the test MR image is collected from the general campus of The Ottawa Hospital, Canada. The manual segmentation is checked by a medical specialist in the hospital. The boundaries of the test and MR images are extracted by the canny edge detector for shape

matching of the test images with the train images. The threshold and sigma are used as the parameters of the canny edge detector. The threshold is 0.5054 and the sigma is 4 for both the test and training images. The threshold is obtained by trial and error method. We tried different threshold and select one which gives longest edges in the image. A simulated annealing optimization technique is used to obtain the best transformation parameters for the global matching (level 0) and for decomposed image matching (level 1 and level 2). The transformation parameters are scaling, rotation, and translation. The scaling is S_x and S_y in x and y directions. The bone in the training images has a size of approximately 170 x 111, and the test image size is 155 x123. The range of the size of the test image used for scaling has 145x 113 as the lower bound and 165 x133 as the upper bound. These dimensions where determined to ensure that the test image scaling range is not be too big or too small, compared to the size of the bone in the training images. The range of the scaling used for the simulated annealing optimization is $0.9354 \leq S_x \leq 1.064$ and $0.9168 \leq S_y \leq 1.081$. The rotation parameter is $-10 \leq \Theta \leq 10$, and in the training images, the translation always starts from (0, 0) to (256,256), in order to find the bone. The translation parameter is $0 \leq t_x \leq 256$ in the x direction and $0 \leq t_y \leq 256$ in the y direction (level 0).

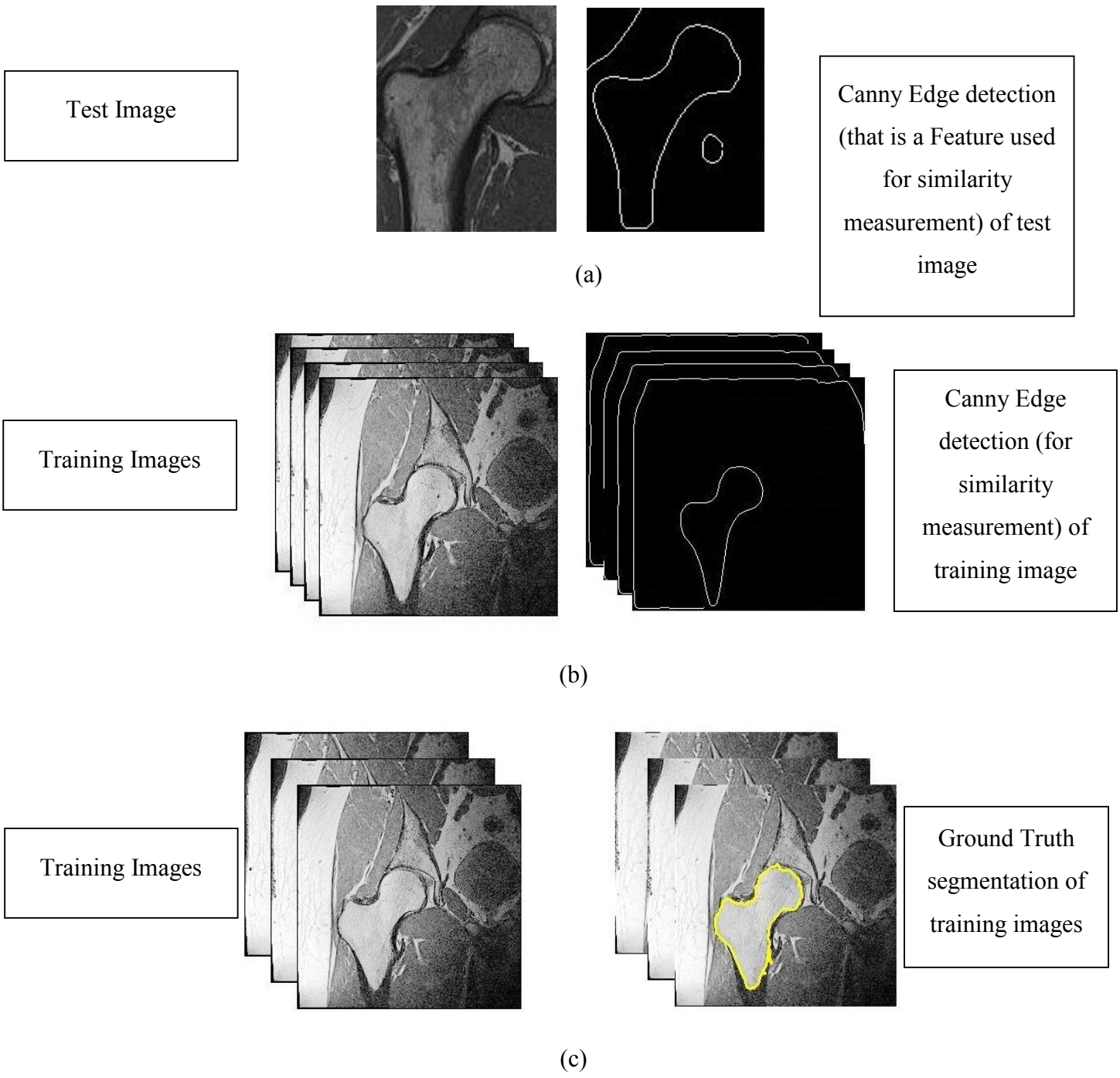

Figure 8: (a) Test image with extracted boundaries (b) Training images database with extracted boundaries (c) Ground truth segmentation in yellow. Note that Canny edges are not the segmentation we aim to obtain, but image feature used as a feature for image similarity.

4.2 Global Matching (Level 0) of Test Image with Database Images.

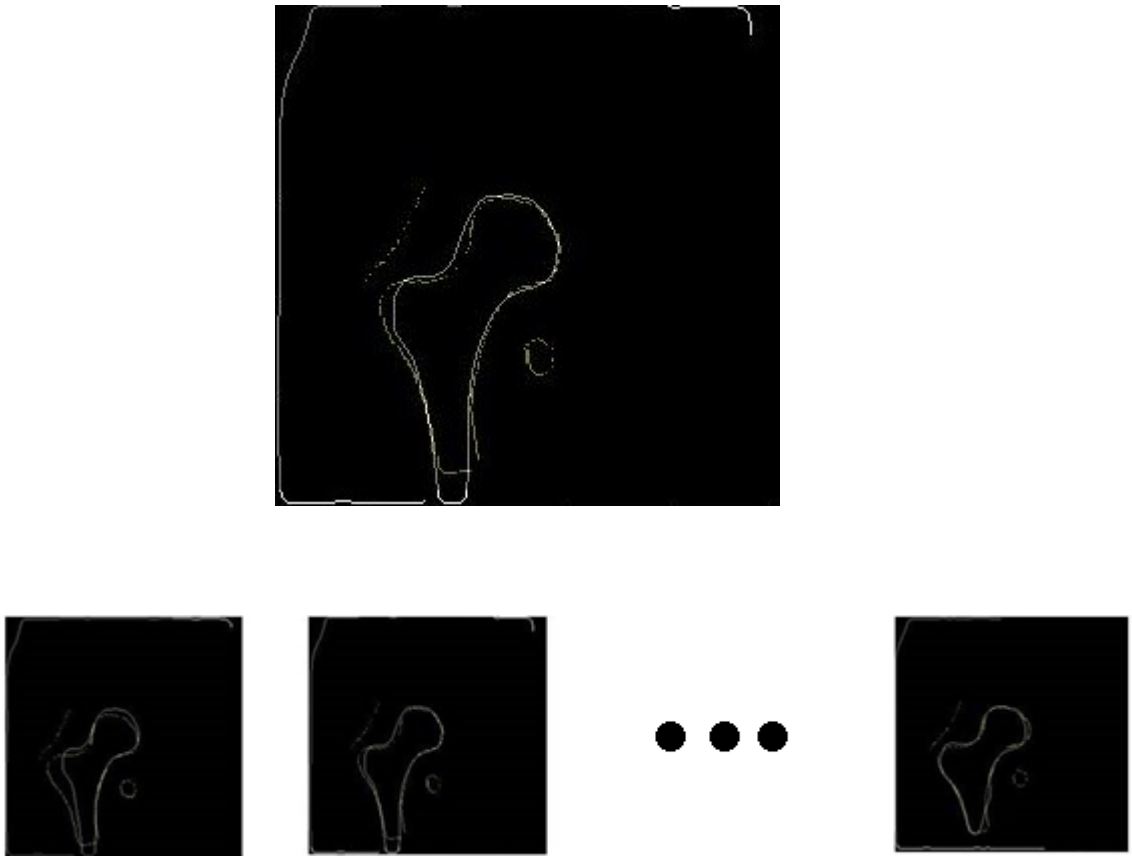

Figure 9: The global matching (level 0) of test images with all the training images. The edges shown are resulted by Canny edge detection and used for image matching.

The test image is matched to the train images, as shown in the above figures. The train images are sorted and selected according to the Hausdorff distance (Similarity metric), as given in the table.

Training Images [IMG]	*Hausdorff Distance (Similarity metric)*	*Scaling* S_X	*Scaling* S_y	*Rotation* Θ	*Translation* t_x	*Translation* t_y
IMG_14	1.2468	0.9696	0.9506	7.8391	35.5126	76.5135
IMG_11	1.2665	0.9867	0.9867	9.7634	30.7097	75.8626
IMG_8	1.2870	0.9605	0.9199	8.0954	37.5502	79.7241
IMG_15	1.4566	0.9364	1.0192	9.9923	30.2818	76.4106
IMG_12	1.4731	1.0402	1.0034	9.6642	29.8776	73.5198
IMG_13	1.6840	0.9697	1.0513	9.4943	30.3255	72.4012
IMG_10	1.6875	0.9360	0.9215	7.1347	37.7186	77.8839
IMG_9	1.8017	0.9933	0.9831	5.1976	40.2992	78.2897
IMG_7	2.0439	0.9980	0.9223	5.1008	42.8955	77.9653
IMG_16	2.2439	1.0573	1.0192	9.9923	28.9102	72.0700
IMG_6	2.8228	0.9455	0.99141	9.9567	28.4911	82.3150
IMG_19	3.8622	1.0088	0.9346	-9.8518	12.1619	87.4600
IMG_20	4.6009	0.9375	0.9284	-3.3757	17.1888	113.4144
IMG_17	4.7993	1.0106	0.9865	7.2046	37.5296	80.8879
IMG_18	4.8739	0.93677	0.9714	-8.9061	11.4982	98.3310
IMG_5	4.8775	1.0288	0.9951	6.6705	35.6191	69.6310
IMG_2	5.0034	1.0577	0.9683	6.0071	35.3834	80.4057
IMG_4	5.1423	0.9369	1.00417	3.2688	40.4894	83.8282
IMG_3	6.2992	0.9977	0.9536	6.0596	35.4705	79.5037
IMG_1	11.0766	0.9355	1.02984	0.0254	0.3791	110.3624

Table 4-1: The similarity metric and transformation parameters obtained after global matching for level 0.

The train images are sorted in ascending order, according to the Hausdorff distance. The top 10 images are selected from the training images database. The selected images are used for the next decomposed part shape matching.

Best matched train images selected for level 1									
IMG_14	IMG_11	IMG_8	IMG_15	IMG_12	IMG_13	IMG_10	IMG_9	IMG_7	IMG_16

4.3 Shape Matching of Level 1 Test Image

Depicted below is the L_0 transformed test image. The total number of transform test images selected for L_0 is 10. For the next level, L_1, each of the L_0 images is decomposed into 4 parts, as shown in Figure 10. The total number of images in L_1 is 40. Now, each of the images of L_1 is matched with selected train images.

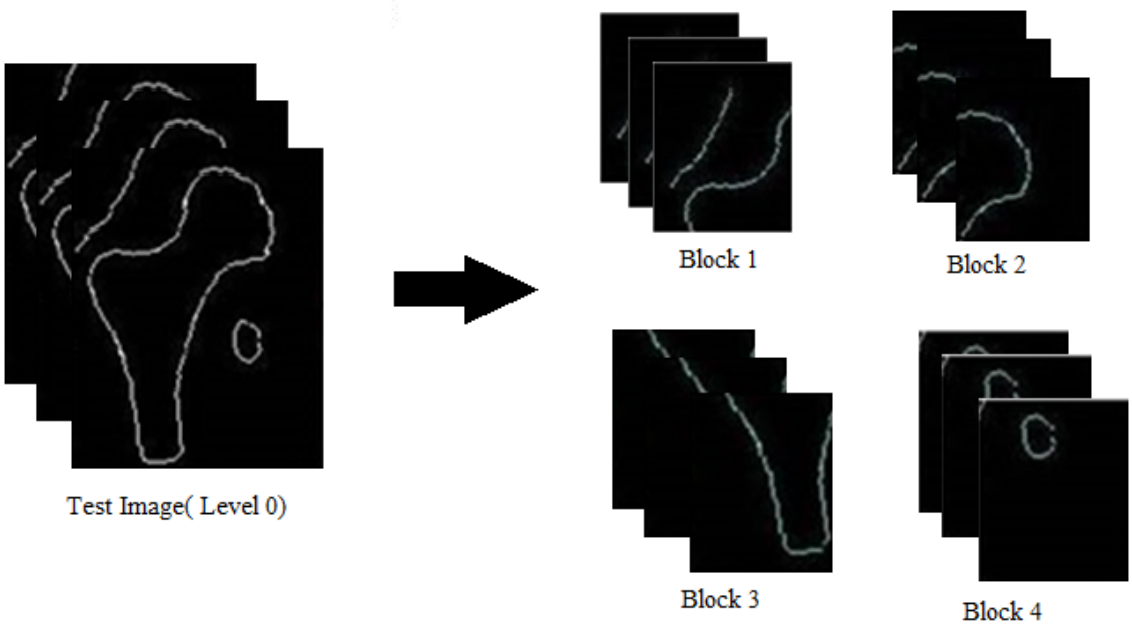

Figure 10: Each of the test images of level 0 is decomposed into four parts and labeled in four blocks. Each block consists of 10 decomposed parts.

4.3.1 Block 1's shape matching with train images

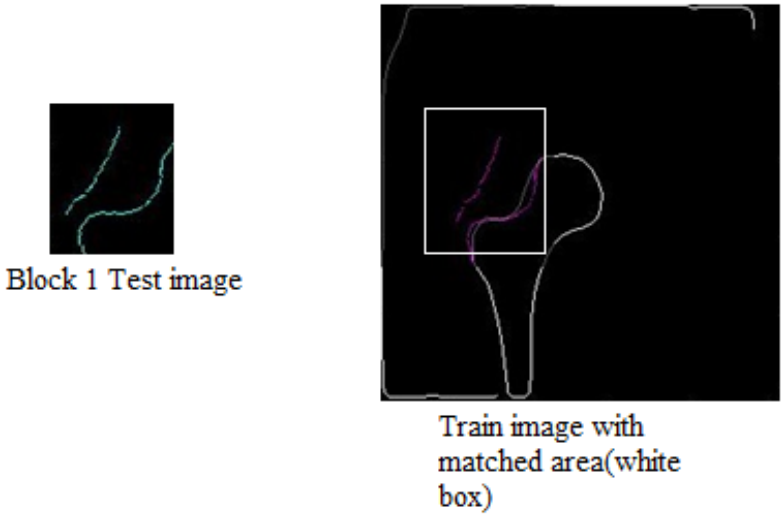

Figure 11: The images show one of the decomposed parts of block 1 and its matched area in the train image.

Training Images [IMG]	*Hausdorff Distance (Similarity metric)*	*Scaling* S_X	*Scaling* S_y	*Rotation* Θ	*Translation* t_x	*Translation* t_y
IMG_14	0.7324	1.0226	0.9553	-4.5110	33.4123	71.3431
IMG_16	0.7579	0.9727	0.9990	-1.6763	29.6046	67.7114
IMG_10	0.8209	1.0123	0.9695	2.0745	38.7268	74.6530
IMG_15	0.8554	1.0124	0.9611	-0.0671	31.7159	71.5321
IMG_13	0.8816	0.9442	0.9724	1.5999	31.8403	72.5675
IMG_12	1.1951	0.9513	0.9605	-3.7906	29.1703	70.4302
IMG_11	1.2600	1.0141	0.9570	1.6810	31.6740	70.5278
IMG_8	1.6164	1.0164	0.9608	2.0923	36.7794	74.6241
IMG_9	1.8500	0.9525	0.9625	4.6967	36.7794	75.7454
IMG_7	2.2029	1.0058	0.9686	3.8429	39.2166	75.4000

Table 4-2: The similarity metric and the transformation parameters obtained for the block 1 matching of level 1.

Best matched training images selected for level 2 (Block1, Block2, Block3, Block4)				
IMG_14	IMG_16	IMG_10	IMG_15	IMG_13

4.3.2 Block 2 test image shape matching

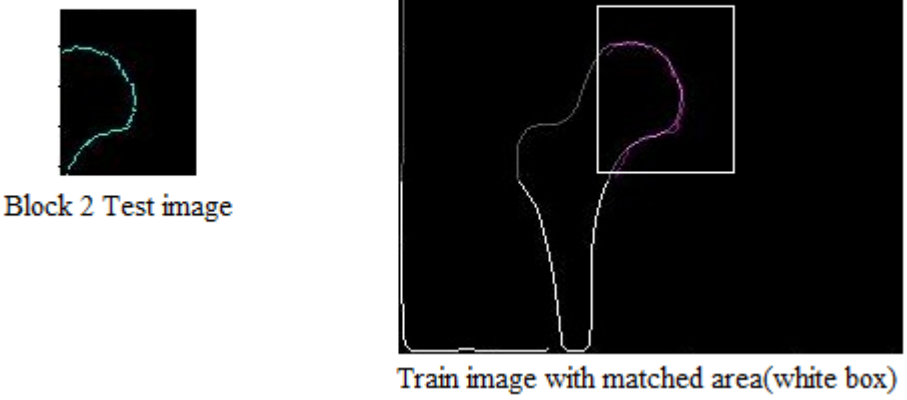

Figure 12: The images show one of the decomposed part of block 2 and its matched area in the train image.

Training Images [IMG]	*Hausdorff Distance (Similarity metric)*	*Scaling* S_X	*Scaling* S_y	*Rotation* Θ	*Translation* t_x	*Translation* t_y
IMG_16	0.3333	0.9472	0.94065	-4.1356	102.0877	74.2950
IMG_8	0.3750	1.0027	0.9422	2.4864	103.3751	75.3979
IMG_12	0.3836	1.0266	0.9757	-0.2089	103.5203	72.7359
IMG_14	0.3971	0.9738	0.8716	0.2005	104.2513	74.5188
IMG_7	0.4407	1.0076	1.0024	0.9359	104.3816	77.6494
IMG_10	0.4516	1.0559	0.9950	2.7117	102.4916	75.1483
IMG_11	0.5161	0.9847	0.9595	-0.1376	105.6734	75.5081
IMG_13	0.5833	1.0441	0.9407	-0.1353	102.4719	74.4986
IMG_15	0.6190	1.0024	0.9529	-0.7610	103.0034	74.5537
IMG_9	1	0.9737	0.9298	-2.2616	105.2864	76.5195

Table 4-3: The similarity metric and the transformation parameters obtained for the block 2 matching of level 1.

Best matched train images for level 2 (Block 5, Block 6, Block 7, Block 8)				
IMG_16	IMG_8	IMG_12	IMG_14	IMG_7

4.3.3 Block 3 test image shape matching

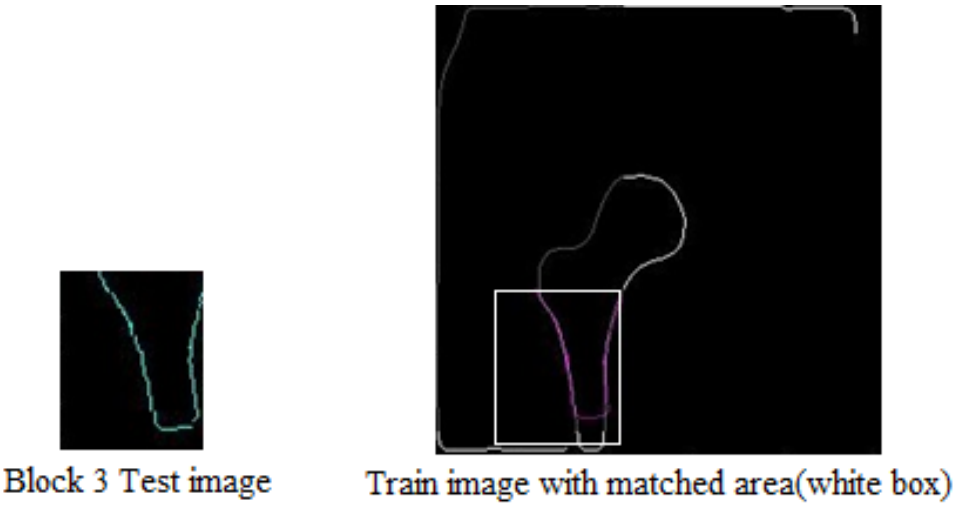

Figure 13: The images show one of the decomposed parts of block 3 and its matched area in the train image.

Training Images [IMG]	*Hausdorff Distance (Similarity metric)*	*Scaling* S_X	*Scaling* S_y	*Rotation* Θ	*Translation* t_x	*Translation* t_y
IMG_11	0.2917	1.0063	0.9366	-0.4973	34.4252	163.8678
IMG_8	0.2982	0.9712	0.9798	0.0658	35.9184	159.3447
IMG_7	0.3478	0.9487	0.9461	0.0428	43.9155	159.8422
IMG_9	0.3679	0.9962	0.9312	0.2586	41.3594	161.4095
IMG_10	0.4021	0.9339	1.00153	0.3815	36.2015	162.4918
IMG_12	0.4662	1.0259	0.9530	1.0071	31.6762	160.7675
IMG_13	0.5796	1.0407	0.9963	0.4138	29.5309	157.9680
IMG_15	0.5872	1	1	0	30.2818	162.4106
IMG_14	0.5962	0.9411	0.09676	1.4367	35.5063	164.5977
IMG_16	0.8175	1.0331	1.0107	2.0264	31.4748	165.0981

Table 4-4: The similarity metric and the transformation parameters obtained for the block 3 matching of level 1.

Best matched train image for level 2 (Block 9, Block 10, Block 11, Block12)				
IMG_11	IMG_8	IMG_7	IMG_9	IMG_10

4.3.4 Block 4 test image shape matching

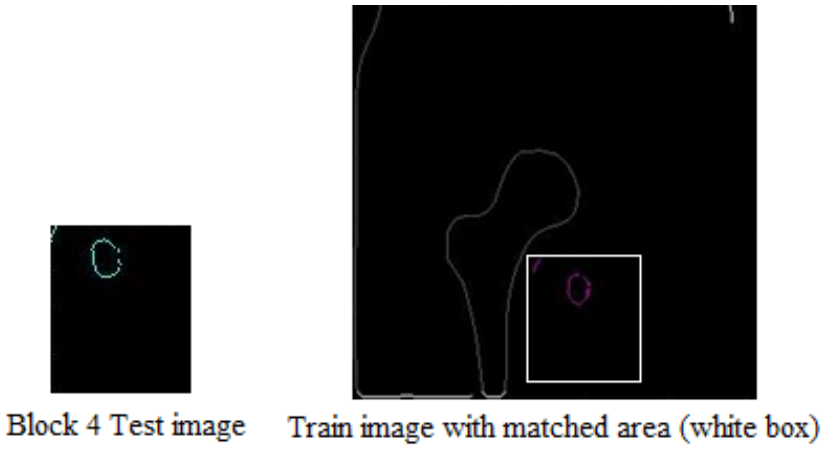

Figure 14: The images show one of the decomposed parts of block 1 and its matched area in the train image.

Training Images [IMG]	*Hausdorff Distance (Similarity metric)*	*Scaling* S_X	*Scaling* S_y	*Rotation* Θ	*Translation* t_x	*Translation* t_y
IMG_ 9	2	0.9749	0.9778	1.6392	109.6572	163.8814
IMG_14	2	1.1165	1.0706	0.2041	105.5391	157.2967
IMG_8	2.1875	0.9456	1.0051	4.7112	106.6476	167.0201
IMG_7	2.400	0.9483	1.0382	-2.8338	111.1753	162.9275
IMG_10	2.6957	0.9918	1.0008	-2.9788	106.0109	162..8529
IMG_13	2.800	0.9987	0.9419	3.8366	110.7702	158.4836
IMG_11	3.2500	1.0285	0.9338	0.9355	104.6365	158.4637
IMG_16	3.2727	0.9434	0.9971	-0.7972	108.9920	165.7255
IMG_15	3.4400	1.0322	0.9593	-1.1351	112.2789	157.4238
IMG_12	3.8519	0.9933	0.9358	-1.3295	104.0671	163.3370

Table 4-5: The similarity metric and the transformation parameters obtained for the block 4 matching of level 1.

Best matched train image for level 2 (Block 13, Block 14, Block 15, Block16)				
IMG_9	IMG_14	IMG_8	IMG_7	IMG_10

The best train image parts after level 1 are shown in the figure below.

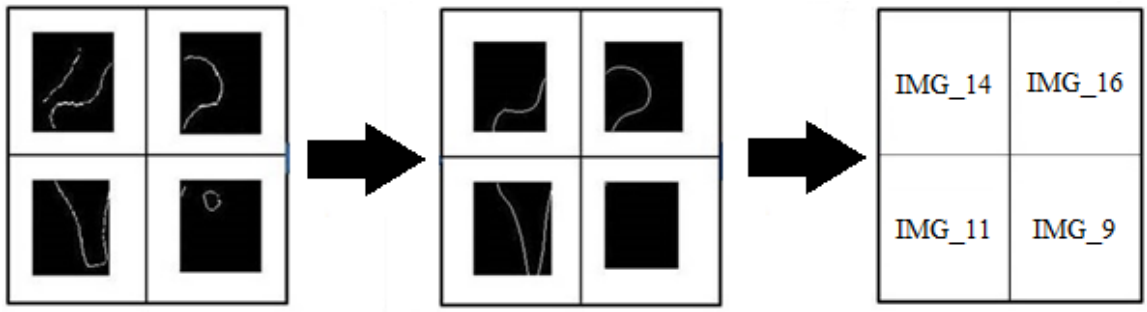

(a) (b) (c)

Figure 15: (a) Test image parts of level 1 (b) Best matched train image parts after level 1 (c) Training images selected after level 1 matching

4.4 Shape Matching of Level 2 Test Images

The test image parts of level 1 are transformed and decomposed further into four parts. For level 2, the decomposed parts are matched over the selected train images. The parts of level 2 (Block 1, Block 14, Block 15, Block 16) with homogeneous intensities are not registered with the selected train images. A rigid transformation (rotation and translation) is used for the shape registration of level 2.

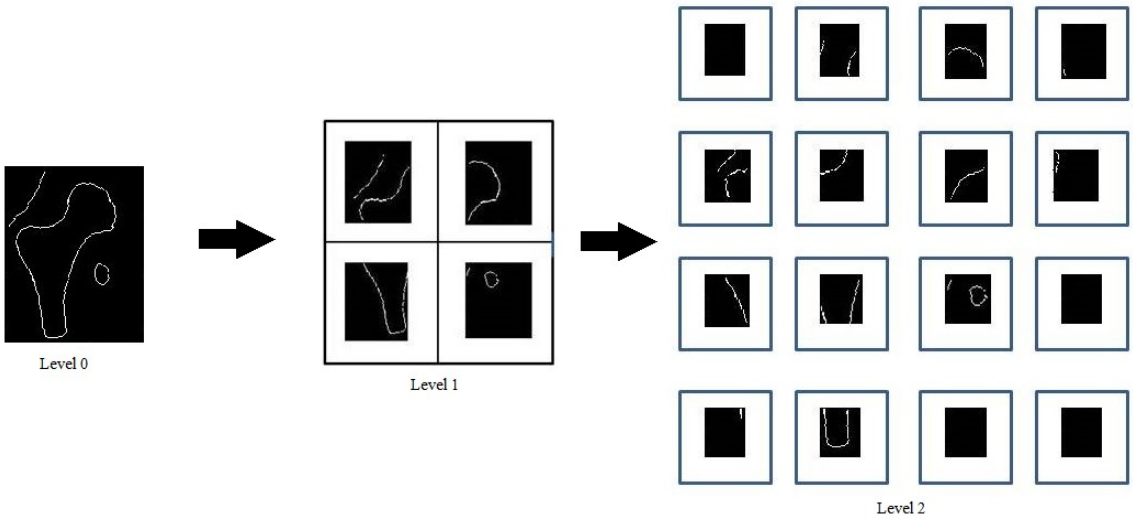

Figure 16: The above figure shows the decomposition of the test image at levels 1 and 2.

4.4.1 Block 1 test image shape matching

The images of block 1 are homogeneous in nature. The matching of the block 1 image is not possible.

4.4.2 Block 2 test image shape matching

Below is the table for the similarity measures and the transformation parameters obtained by matching the block 2 test images with selected training images.

Training Images [IMG]	*Hausdorff Distance (Similarity metric)*	*Rotation* Θ	*Translation* t_x	*Translation* t_y
IMG_10	**0.4500**	**-2.8669**	**69.1500**	**76.5711**
IMG_15	0.5000	-2.6469	66.4446	71.2301
IMG_13	0.6100	-4.7209	68.7424	70.1383
IMG_14	0.6667	-4.1055	92.783	88.5085
IMG_16	1.8095	-3.9638	72.4557	63.1780

Table 4-6: Similarity metric and transformation parameters obtained for block 2 of level 2.

4.4.3 Block 3 test image shape matching

The table of the similarity measures and transformation parameters obtained by matching block 3 test images with selected training images.

Training Images [IMG]	*Hausdorff Distance (Similarity metric)*	*Rotation* Θ	*Translation* t_x	*Translation* t_y
IMG_10	**0.500**	**-1.5492**	**38.4611**	**117.0197**
IMG_14	0.8649	4.7345	33.813	116.5236
IMG_13	1.4167	3.5560	31.542	115.1655
IMG_16	1.6154	2.9426	27.9177	118.5184
IMG_15	3.1563	2.8391	28.1456	116.219

Table 4-7: Similarity metric and transformation parameters obtained for block 3 of level 2.

4.4.4 Block 4 test image shape matching

The table of the similarity measures and transformation parameters obtained by matching block 4 test images with selected training images.

Training Images [IMG]	*Hausdorff Distance (Similarity metric)*	*Rotation* Θ	*Translation* t_x	*Translation* t_y
IMG_14	**0.2593**	**1.9894**	**71.1498**	**118.1277**
IMG_13	0.2941	-4.7966	68.5109	116.8451
IMG_10	0.3125	-2.9105	70.2301	118.4842
IMG_15	0.4103	3.8455	68.0159	113.2105
IMG_16	0.4848	2.0608	0.0981	1.5226

Table 4-8: Similarity metric and transformation parameters obtained for block 4 of level 2.

4.4.5 Block 5 test image shape matching

The table of the similarity measures and transformation parameters obtained by matching block 5 test images with selected training images.

Training Images [IMG]	*Hausdorff Distance (Similarity metric)*	*Rotation* Θ	*Translation* t_x	*Translation* t_y
IMG_7	**0.1667**	**-1.2123**	**105.2344**	**78.4266**
IMG_14	0.2647	4.5823	101.972	73.5457
IMG_8	0.2727	0.1331	100.6398	74.2683
IMG_16	0.4643	2.1098	100.5857	73.3154
IMG_12	0.6111	4.9848	99.6384	70.1222

Table 4-9: Similarity metric and transformation parameters obtained for block 5 of level 2.

.

4.4.6 Block 6 test image shape matching

The table of the similarity measures and transformation parameters obtained by matching block 6 test images with selected training images.

Training Images [IMG]	*Hausdorff Distance (Similarity metric)*	*Rotation* Θ	*Translation* t_x	*Translation* t_y
IMG_8	**0**	**-0.8997**	**136.3751**	**70.5873**
IMG_16	0.016	-1.5083	141.1442	70.2019
IMG_7	0.0769	3.1654	133.3972	74.1234
IMG_14	0.1250	0.4795	136.4670	69.4635
IMG_12	0.2857	-2.3429	139.9147	67.4572

Table 4-10: Similarity metric and transformation parameters obtained for block 6 of level 2.

4.4.7 Block 7 test image shape matching

The table of the similarity measures and transformation parameters obtained by matching block 7 test images with selected training images.

Training Images [IMG]	*Hausdorff Distance (Similarity metric)*	*Rotation* Θ	*Translation* t_x	*Translation* t_y
IMG_14	**0.0370**	**2.3447**	**99.8383**	**121.7256**
IMG_7	0.0909	2.1834	99.1275	123.1555
IMG_8	0.1724	1.7581	4.1749e	123.8329
IMG_16	0.5490	2.9217	100.3879	122.1374
IMG_12	0.8400	0.1509	102.4249	121.3503

Table 4-11: Similarity metric and transformation parameters obtained for block 7 of level 2.

4.4.8 Block 8 test image shape matching

The table of the similarity measures and transformation parameters obtained by matching block 8 test images with selected training images.

Training Images [IMG]	*Hausdorff Distance (Similarity metric)*	*Rotation* Θ	*Translation* t_x	*Translation* t_y
IMG_8	**0**	**4.0686**	**138.5775**	**118.4133**
IMG_16	0.025	-4.6325	139	121.4573
IMG_7	0.0556	-4.8784	133.493	121.0863
IMG_12	0.1429	-1.3782	141.4405	119.7362
IMG_14	0.2000	-0.3414	136.5205	120.177

Table 4-12: Similarity metric and transformation parameters obtained for block 8 of level 2.

4.4.9 Block 9 test image shape matching

The table of the similarity measures and transformation parameters obtained by matching block 9 test images with selected training images.

Training Images [IMG]	*Hausdorff Distance (Similarity metric)*	*Rotation* Θ	*Translation* t_x	*Translation* t_y
IMG_9	**0.1367**	**2.4756**	**38.5782**	**160.1957**
IMG_7	0.1600	-0.1812	43.5387	159.08
IMG_11	0.2000	-2.4902	33.5003	163.8823
IMG_10	0.3810	4.1947	32.8055	158.4195
IMG_8	0.6667	-4.0398	35.464	156.176

Table 4-13: Similarity metric and transformation parameters obtained for block 9 of level 2**.**

4.4.10 Block 10 test image shape matching

The table of the similarity measures and transformation parameters obtained by matching block 10 test images with selected training images.

Training Images [IMG]	*Hausdorff Distance (Similarity metric)*	*Rotation* Θ	*Translation* t_x	*Translation* t_y
IMG_8	**0.0012**	**0.4538**	**71.2815**	**159.5171**
IMG_7	0.0435	2.7245	74.4148	161.2832
IMG_9	0.1034	-1.9161	76.3613	156.6866
IMG_10	0.1250	3.7585	71.0586	163.762
IMG_11	0.1429	0.7702	68.8753	161.7878

Table 4-14: Similarity metric and transformation parameters obtained for block 10 of level 2.

4.4.11 Block 11 test image shape matching

The table of the similarity measures and transformation parameters obtained by matching block 11 test images with selected training images.

Training Images [IMG]	*Hausdorff Distance (Similarity metric)*	*Rotation* Θ	*Translation* t_x	*Translation* t_y
IMG_7	**0**	**2.6604**	**44.2459**	**198.5744**
IMG_8	NaN	0	0	0
IMG_9	NaN	0	0	0
IMG_10	NaN	0	0	0
IMG_11	NaN	0	0	0

Table 4-15: Similarity metric and transformation parameters obtained for block 11 of level 2.

4.4.12 Block 12 test image shape matching

The table of the similarity measures and transformation parameters obtained by matching block 12 test images with selected training images.

Training Images [IMG]	*Hausdorff Distance (Similarity metric)*	*Rotation* Θ	*Translation* t_x	*Translation* t_y
IMG_7	**0.3148**	**-4.0346**	**74.4615**	**200**
IMG_9	0.4035	-0.7871	74.8111	202.0662
IMG_10	0.4706	-1.1726	70.5198	199.6909
IMG_11	0.5769	1.2965	68.5022	204.7034
IMG_8	0.5833	0.0565	70.6922	201.7206

Table 4-16: Similarity metric and transformation parameters obtained for block 12 of level 2.

4.4.13 Block 13 test image shape matching

The table of the similarity measures and transformation parameters obtained by matching block 13 test images with selected training images.

Training Images [IMG]	*Hausdorff Distance (Similarity metric)*	*Rotation* Θ	*Translation* t_x	*Translation* t_y
IMG_8	**17.3200**	**-0.5547**	**101.5682**	**161.2734**
IMG_10	18.7250	0	101	157
IMG_9	20.8409	0	104	158
IMG_7	24.1613	1.0119	106.6625	157.5226
IMG_14	NaN	0	0	0

Table 4-17: Similarity metric and transformation parameters obtained for block 13 of level 2.

4.4.14 Block 14 test image shape matching

The images of block 14 are homogeneous in nature. Matching the block 14 images is therefore not possible.

4.4.15 Block 15 test image shape matching

The images of block 15 are homogeneous in nature. Matching the block 15 images is therefore not possible.

4.4.16 Block 16 test image shape matching

The images of block 16 are homogeneous in nature. Matching the block 16 images is therefore not possible.

Best matched training images selected after level 2	
Block Number of Level 2	Best Matched Training Image
1	Null
2	IMG_10
3	IMG_10
4	IMG_14
5	IMG_7
6	IMG_8
7	IMG_14
8	IMG_8
9	IMG_9
10	IMG_8
11	IMG_7
12	IMG_7
13	IMG_7
14	Null
15	Null
16	Null

Table 4-18: The best training images for each of the blocks after level 2.

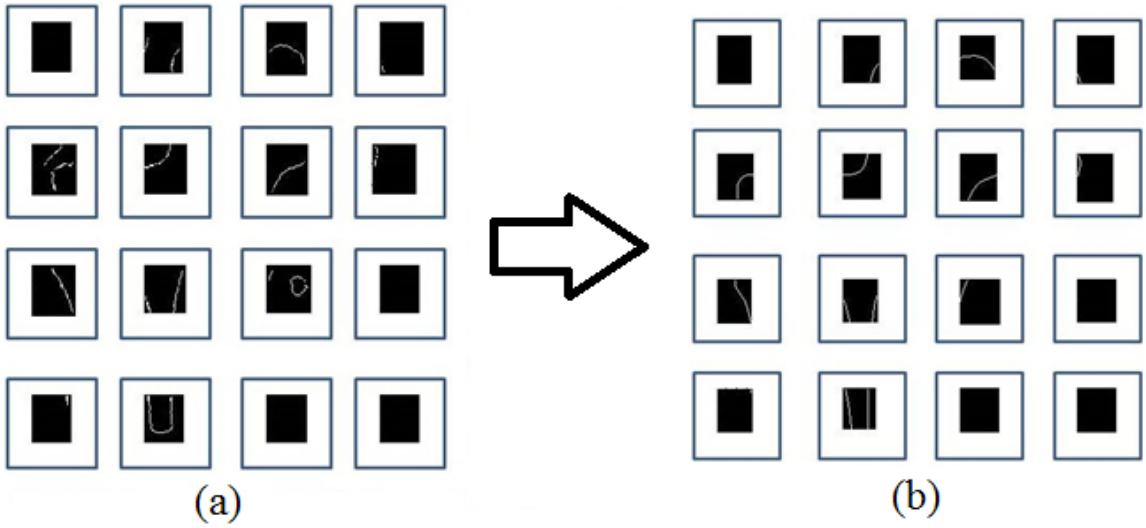

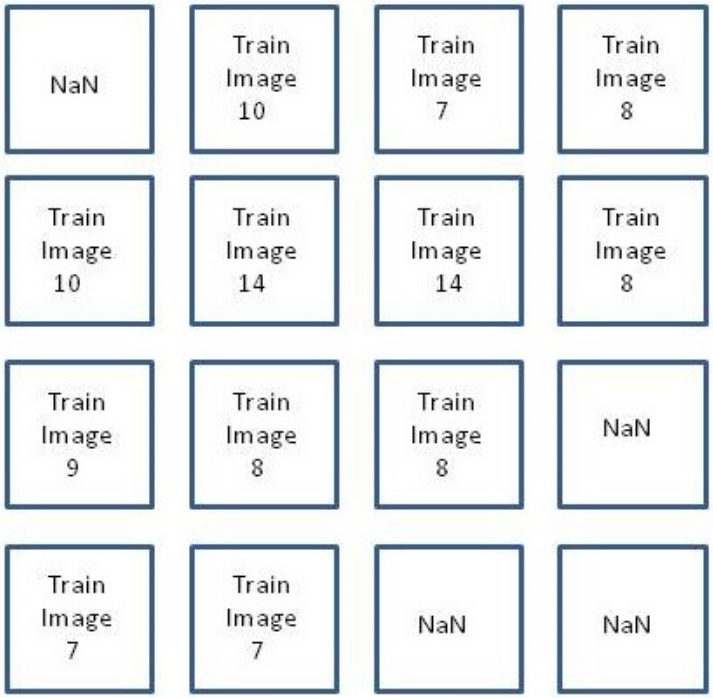

Figure 17: (a) Test image parts of level 2 (b) Best matched training image parts after level 2 (c) Training images selected after level 2 matching.

4.5 Re-Composition Process to Build Mosaic of Training Image Parts

The training image parts are cropped the size of the test image parts. They are cropped based on the translation parameters obtained from the decomposed registration of the test parts with the training images. The list of the corresponding best training image parts for each of the test image parts is shown in Table 4.18, but only the matching parts are shown.

As shown above, the best training image parts are cropped to the corresponding test image part. Now, each of the training image parts is inversely transformed to obtain the mosaic of the training image, which matches the original test image. The parameters of the training image parts, obtained from level 2 of the decomposed part registration, are transformed inversely. The inverse of the scaling parameters is $1/S_x$ and $1/S_y$, the inverse rotation is the negative of the angle of rotation Θ, the inverse of the translation is $-t_x$ and $-t_y$. At each level, the best training image is transformed until it reaches level 0.

Once the test image is represented as collection of best matched training images as in shown in Figure 19 with any feature for image matching. The ground truth segmentation is transferred from training images to the give test image.

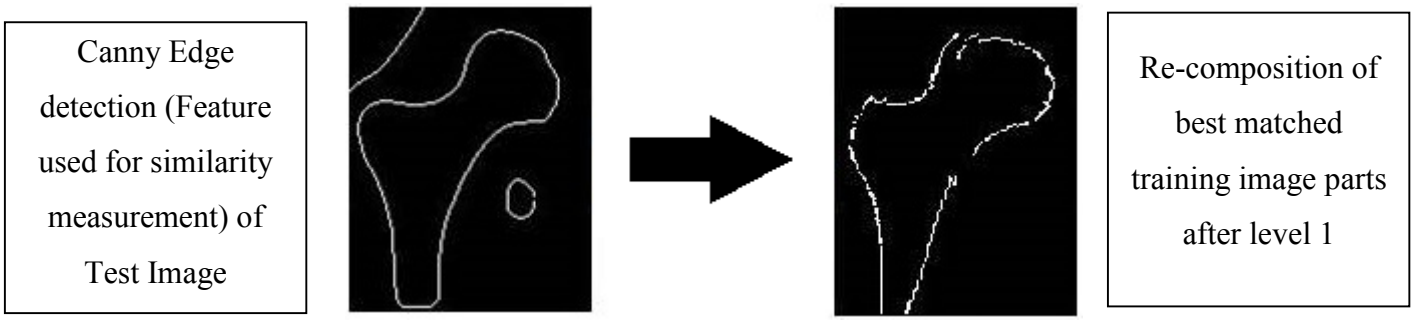

Figure 17: (a) Test image (edge image) (b) Mosaic of the best matched training image parts after level 1.

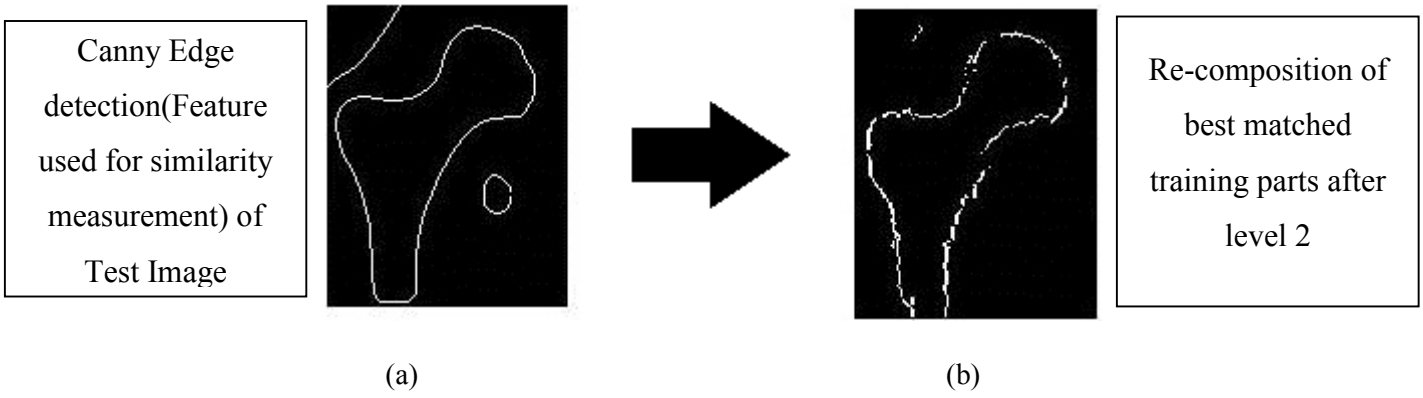

Figure 18: (a) Test image (b) Mosaic of the best matched training image parts after level 2.

The above figure shows that the test image is the collection of the best parts of the training image.

Original Test Image

Re-composition of best matched training images

(a) (b)

Figure 19: (a) Original test image (b) Mosaic of the best matched training image parts after level2

(a) **(b)**

Figure 20: (a) Original test image (b) Ground truth segmentation from a set of best matching training images are transferred to the test image in its original space (segmentation in yellow).

As mentioned above, at every level of the pyramid decomposition, we find the best training image parts, which are matched with the test image. At level 0, the training image 14 (IMG_14) is the best matched training image. At level 0, the similarity of the re-composition of the training image and the test image, measured in terms of the

Hausdorff distance, is 1.9880. At level 1, the recomposed image consists of the four best matched training images. The Hausdorff distance between the recomposed image and the test image is 1.4521. At level 2, the recomposed image consists of the 16 best matched training images and the Hausdorff distance between the recomposed image and the test image is 1.2981. As we can see, the Hausdorff distance improves as we increase in the levels, which consolidates the idea that as we go on to deeper levels, the recomposed image is more similar to the test image. The manual segmentation is transferred from the database of the training image to the corresponding location in the test image.

The automatic segmentation is implemented on the test image. The threshold based segmentation (Otsu method) is applied on the test image, and the results are shown in Figure 21. The threshold based segmentation consists of the holes in the final segmentation of the test image. The holes can be improved by applying morphological operations to the segmentation. The model based segmentation is implemented on the test image, for instance active contour. An active contour based segmentation (Chan Vese method) uses the mask that defines the initial state of the active contour. The active contour segmentation of the test image is shown in Figure 22. The automatic segmentation seems to be correct but medically it is not. The experts still correct the automatic segmentation and determine the abnormal shape in the hip joint structure. The automatic segmentation does not care about the abnormality in the shape of the bone.

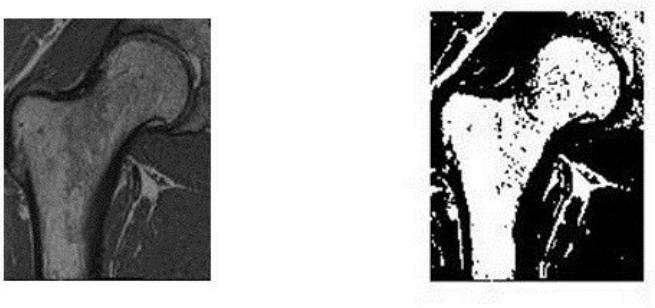

(a) **(b)**

Figure 21: (a) Original test image (b) Threshold based segmentation of test image

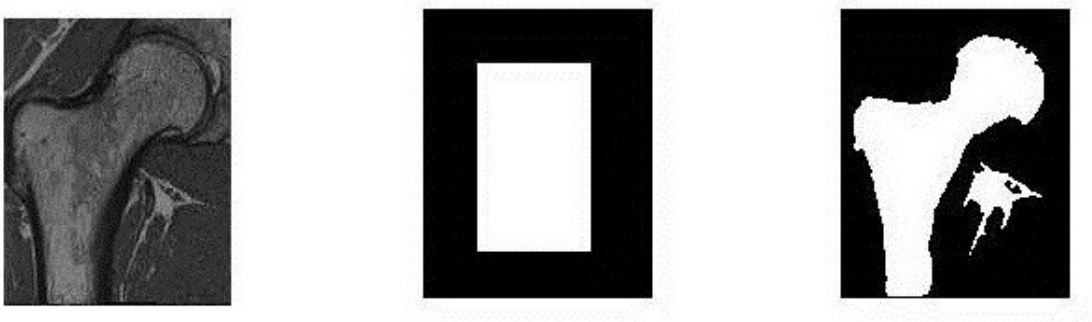

(a) **(b)** **(c)**

Figure 22: (a) Original test image (b) Mask for active contour segmentation (c) Active contour segmentation

In our approach, we extracted the edge as a feature to find the similarity between a test image and the training images. We can also use other features like SIFT, SURF, Harris corner detector and many more. We determine the edge features of the test image that are most similar to the edge features of the training images. At level 2, the best matched training images are cropped the same size as the test image part and transformed inversely to create a mosaic. The mosaic consists of the edge of the best training image parts, which represent the edge image of the test image. Now, the manual segmentation of the training image is transferred to the original test image, in its corresponding

location. We have applied our algorithm to two test images and the results are shown in Figure 23 and Figure 25.

Test Image 1

Segmentation of test image after applying our algorithm

(a) **(b)**

Figure 23: (a) Test image 1 (b) Ground truth segmentation transferred to test image from database of training image

(a) (b)

Figure 24: (a) Original test image 2 (b) Mosaic of best matched training image parts after level2

Test Image 2

Segmentation of test image after applying our algorithm

(a) **(b)**

Figure 25: (a) Test image 2 (b) Ground Truth Segmentation transferred to test image from database of training image

4.6 Discussion

In our present work, we were able to improve automatic segmentation of femur bone in MR images by transferring experts' segmentation from a set of training images in

database to a given test image. Our method represents a test image as a re-composition of best-matched training image parts. The results show that Hausdorff distance between re-composed image and the original test image decreases over the levels of pyramid decomposition. The deeper level re-composition provides more similarity to the input test image. The similar kind of shape matching approach used to select the best training image part for human detection and segmentation can be found in [6] [62] but our segmentation approach is different from this work. They used chamfer matching algorithm for shape matching and their algorithm does not transform image to obtain perfect matching.

In our experiment an expert's segmentation is transferred to the corresponding location in the test image, but any information in the training images can be transferred to the test image with the same principle. So if a doctor wants to draw a medically meaningful segmentation even though it may not correct in term of image intensity, it is possible in our methods. If a doctor wants to transfer some coloring on certain organ (e.g. draw a liver in red), it is also possible in our methods. Here we emphasize the fact that we can provide medically correct segmentation for surgical treatments not only relying on intensity if the database is made in the way. What we are able to transfer to a test image is the information imbedded in training images.

Medical image segmentation has remained a challenging problem because of non-uniform intensity distribution in the image and there is no exact solution for segmentation of object in medical images. In [30], the segmentation of abdominals in MR image is done by a texture feature based seeded region growing algorithm, however, for this

approach to work, texture homogeneity is necessary. Most of the existing method based on intensity attributes needs intensity homogeneity for good segmentation, otherwise it leads to problems of holes and over-segmentation. On the other hand, shape prior knowledge is used to segment MR hip joint structure in [9] [11]. Unfortunately, some results are unsatisfactory due to the improper atlas to affine registration; and the results are checked by Dice's similarity coefficient. In our work, we checked Hausdorff similarity metric at each level and reject half of the image (those with low Hausdorff distance), in order to avoid unsatisfactory results in the re-composition stage. We performed validation of our method at each level by calculating the Hausdorff similarity between the re-composition image at a particular level and the original test image. Therefore, checking similarity in both decomposition and the re-composition stage provides the robustness in an algorithm. Our experiment has been limited due to the small dataset that only consists of CAM type abnormality images.

We have presented the final result, which solves the problem of holes and over-segmentation, in which the segmentations are medically correct compared to existing medical image segmentation methods. The segmentation from existing methods might result to be correct in terms of intensity, but it does not guarantee to be medically correct. In practice many times a medical expert has to correct segmentation obtained from existing methods, prior to surgical treatment. Contrarily our method solve this problem using database of medically correct segmentation.

Finally, our finding demonstrates a method transferring expert's knowledge from training image to a test image. The knowledge transfer is accomplished by representing test image

with a mosaic of the best matching training image parts. We observed that as similarity increases between recomposed image and test image, at every level, it improves the final segmentation of test image. Our work not only applies to medical images but can also have various other applications. This work proves that an automatic algorithm can replicate like expert's segmentation. Given the known benefits of the algorithm, a future study to improve it for the segmentation of all type abnormalities in hip-joint structure would be very valuable.

Chapter 5 : Conclusion

In this thesis, we used database of training images and image matching techniques to solve the problem of segmenting the femur bone in the hip joint MR images. The main idea of the research work is to represent the unknown image as a collection of the best matched training images. Medical expert knowledge is transferred from best training image parts to the unknown test image. The key idea of the approach is based on the pyramid decomposition shape matching of a test image with the database of MR training images, where each of the best matched training parts is transformed inversely to represent the test image from the collection of training image parts.

The method has two stages, the first being the pyramid decomposition to match the test image with the training image database. The shape matching is based on the Hausdorff distance algorithm to obtain the transformation for which the Hausdorff distance is minimal. The training images are sorted in ascending order based on the Hausdorff distance obtained from shape registration; at each level, half of the training images are selected. The decomposition of the test image is conducted until level two. The final results of first stage provide the best training image part for each block at level 2.

The second stage is the reverse of the above step; it is the re-composition approach to create the test image from the best training image parts. The transformation parameters obtained from the pyramid decomposition are used for the best training image parts. They undergo an inversion, which is applied to each of the best training image parts. The final result of stage two is the mosaic of the best matching training image parts, and the medical expert segmentation is transferred from the best training parts to the corresponding location in the original test image.

We conducted the experiments with real MR images. The method is applied on the MR images of a hip joint structure to obtain the segmentation of the femur. The segmentation of the hip joint is a challenging task because of the dissimilarity between various patients' bones. The different MR images have distinctive intensity variations due to the digital imaging system. Our method shows the good results obtained when representing the test image with the collection of the best matched training image parts. As we go deeper into the pyramid structure, the mosaic becomes more similar to the original test image.

The major contributions of our work are:

- *Use of expert knowledge*: We have found this novel approach where experts' knowledge is transferred from a database (training images) to a test image. The method is applied on the MR images of hip-joint structures to solve the problem of femur segmentation.

- *Application of the system to solve different segmentation problems*: The method is not only applicable to the femur bone segmentation of the MR image, but can also be applied to other types of images for various segmentation problems.

Although the results were convincing, a major drawback of this method is a sparsely populated training image database for the pyramid decomposition. The method only uses the shape information of the object for the image matching. In the future, we will increase the training image database and use both the intensity and the shape matching to find a best matching image parts.

Our final results have not been verified by an expert, which would allow us to improve the methods in future. Besides comparing results with expert's segmentation, we also intend to increase the database of training images with all type of FAI from various patients. A larger database increases the scope of the algorithm for segmentation of different types of FAI. It would be interesting to see and compare results produced by changing features and similarity metric (e.g. chamfer distance, shape context, SIFT, Harris corner) in our algorithm.

References

[1] A. Chavez Aragon, W. Lee and A. Vyas, "A crowdsourcing web platform-hip joint segmentation by non-expert contributor," in *IEEE International symposium on medical measurement and applications proceedings*, 2013.

[2] S. Wisniewski and G.B., "Femoroacetabular impingement : An overlooked cause of hip joint," *American journal of physical medicine and rehabilitation,* no. 85, pp. 546-549, 2006.

[3] W. Rucklidge, "Efficiently locating objects using Hausdorff distance," *International journal of computer vision,* vol. 24, pp. 251-270, 2006.

[4] Priyadarshi and D. S.Selvathi, "Survey on segmentation of liver from CT images," in *IEEE conference on advanced communication control and computing technologies*, 2006.

[5] J. X. Knag, N. M. Qi and Jian-Hou, "A hybrid method combining Hausdorff distance, genetic algorithm and simulated annealing for image matching," in *IEEE conference on computer modelling and simulation*, 2006.

[6] Zhe Lin and L. Davis, "Shape-based human detection and segmentation via hierarchical part-template matching," in *IEEE transaction on pattern analysis and machine intelligence*, 2006.

[7] M. Ansari and R. Anand, "Region based segmentation and image analysis with application to medical imaging," in *International conference on information and communication technology in electrical sciences*, 2007.

[8] R. Inamdar and D. Ramdasi, "Active appreance model for segmentation of cardiac MRI data," in *International conference on communication and signal processing*, 2013.

[9] D. Kainmueller, H. Lamecker, S. Zachow and H. Hege, "An articulated statistical shape model for hip joint segmentation," in *International conference of IEEE EMBS*, 2009.

[10] S. Angelina, L. Suresh and S. Veni, "Image segmentation based on genetic algorithm for region growth and region merging," in *International conference on computing, electronics and electrical technologies*, 2006.

[11] Y. Xia, S. Chandra, O. Salvado and J. Fripp, "Automated MR hip bone segmentation," in *International conference on digital image computing technqiues and applications*, 2011.

[12] J. Pardo, D. Cabello and J. Heras, "A snake for model based segmentation of biomedical images," in *Elsevier pattern recognition letters*, 1997.

[13] S. Vasilache and K. VanNajarian, "A unified method based on wavelet filtering and active contour models for segmentation of pelvic CT images," in *International conference on complex medical engineering*, 2009.

[14] H. Guan, De-yu Li, Jiang-li and W. Tian-Fu, "Segmentation of ultrasound medical image using a hybrid method," in *IEEE international conference on complex medical engineering*, 2007.

[15] J. Zhang, G. Han and Y. Wo, "Image registration based on generalized and mean Hausdorff distance," in *International conference on machine learning and cybernetics*, 2005.

[16] A. Kazerooni, A. Ahmadian, N. Serej, H. Rad, H. Saberi, H. Yousefi and P. Farnia, "Segmentation of brain tumors in MRI images using multi-scale gradient vector flow," in *IEEE International conference of engineering in medicine and biology society*, 2005.

[17] M. Philippon, R. Maxwell, T. Johnston, M. Schenker and K. Briggs, "Clinical presentation of femoroacetabular impingement," in *The official journal of EESKA*, 2007.

[18] L. Zhang, W. XaioJuan and ZanSheng, "A fast image segmentation approach based on level set method," in *International conference on signal processing*, 2006.

[19] L. Michael, W. Robertson and G. Reinhold, "Femoroacetabular impingement: Diagnosis and management including open surgical techniques," in *Elseveir Operative technqiues in sports medicine*, 2007.

[20] [Online] Available: http://www.methodistorthopedics.com/femoroacetabular-impingement-fai.

[21] [Online] Available in http://www.kevinneeld.com/2011/Training-around-femoroacetabular-impingement .

[22] [Online] Available in http://www.hopkinsmedicine.org/healthlibrary/test_procedures/orthopaedic/hip_re.

[23] [Online] Available in http://www.healthpages.org/anatomy-function/hip-structure-function-common- problems.

[24] [Online] Available in http://www.bartleby.com/107/59.html.

[25] [Online] Available in http://teachmeanatomy.info/lower-limb/bones/the-femur.

[26] [Online] Available in http://www.bartleby.com/107/57.html.

[27] J. P. Hornak. [Online] Available in https://www.cis.rit.edu/htbooks/mri/.

[28] R. H. Hashemi, W. G. Bradley and C. J. Lisanti, MRI: The Basics, Lippincott Williams and Wilkins.

[29] D. G. Mitchell and M. Cohen, Magnetic resonance imaging principles, Philadelphia, Pa:Saunder, 2004.

[30] W. Jie, S. Poehlman, M. Noseworthy and M. Kamath, "Texture feature based

automated seeded region growing in abdominal MRI segmentation," in *International conference on biomedical engineering and informatics*, 2008.

[31] B. Senthilkumar, G. Umamaheshwari and J. Karthik, "A novel region growing segmentation algorithm for detection of breast cancer," in *IEEE conference on computational intelligence and computing research*, 2008.

[32] Y. Zhennan, W. Wenhan, Y. Hexin and J. Huang, "Image segmentation on pre-treatment and region growing segmentation method of liver," in *International conference on image and signal processing*, 2010.

[33] W. C. Chang, L. Jiebo and K. Parker, "Image segmentation via adaptive K-mean clustering and knowledge based morphological operations with biomedical applications," in *IEEE transaction on image processing*, 1998.

[34] M. Singh, P. Patel, D. Khosla and T. Kim, " Segmentation of functional K-mean clustering," in *IEEE nuclear science symposium and medical imaging conference*, 1995.

[35] S. Shen, W. Sandham, M. Granat, M. Dempsey and J. Patterson, "Fuzzy clustering based applications to medical image segmentation," in *International conference of the IEEE engineering in medicine and biology society*, 2010.

[36] D. Selvathi and R. Dhivya, "Segmentation of tissue in MR images using modified spatial fuzzy C mean algorithm," in *International conference on signal processing, image processing and pattern recognition*, 2013.

[37] V. Chen and S. Ruan, "Graph cut segmentation technique for MRI brain tumor extraction," in *International conference on image processing theory tools and application*, 2010.

[38] M. Zouqi and J. Samarabandu, "Prostate segmentation from 2D ultrasound images using graph cut and domain knowledge," in *Canadian conference on computer and robot vision*, 2008.

[39] S. Zhuang, N. Tustison, B. Avants and J. Gee, "Adaptive graph cuts with tissue

prior for the brain MRI segmentation," in *IEEE international symposium on biomedical imaging*, 2006.

[40] D. Freedman and T. Zhang, "Interactive graph cut based segmentation with shape prior," in *IEEE society conference on computer vision and pattern recognition*, 2005.

[41] L. Zhentai, F. Qainjian, S. Pencheng and C. Wufun, "Unsupervised segmentation of medical image based on FCM and mutual information," in *IEEE international conference on complex medical engineering*, 2007.

[42] S. Kannan, R. Pandiyarajan and S. Ramathilagam, "Effective weighted bias fuzzy C-mean in segmentation of brain MRI," in *International conference on intelligent and advanced systems*, 2010.

[43] ShangLing, l. Chao, G. Haibing and A. Abraham, "Fuzzy C-mean with wavelet filteration for MR image segmentation," in *Sixth world congress on nature and biologically inspired computing*, 2014.

[44] J. Jiayan, Z. Songfeng, A. Toga and T. Zhuowen, "Learning based coarse to fine image registration," in *IEEE conference on computer vision and pattern recognition*, 2008.

[45] D. Freedman and T. Zhang, "Interactive graph cut based segmentation with shape priors," in *IEEE computer society conference on computer vision and pattern recognition*, 2005.

[46] N. Birkbeck, D. Cobzas, M. Jagersand and A. Murtha, "An interactive graph cut method for brain tumor segmentation," in *Workshop on application of computer vision*, 2009.

[47] Y. Faliu and M. Inkyu, "Image segmentation: A survey of graph cut methods," in *International conference on systems and informatics*, 2012.

[48] A. Gharipour and A. Liew, "An intergration strategy based on fuzzy clustering nd level set method for cell image segmentation," in *IEEE international*

conference on signal processing, communication and computing, 2013.

[49] K. Cheng, G. Lixu, W. Jianghua and J. Xu, "A novel set based shape prior for liver segmentation from MRI images," in *International workshp on medical imaging and augmented reality*, 2008.

[50] A. Bardera, M. Feixas, I. Boada, J. Rigau and M. Sert, "Medical image registration based on BSP and quad tree partitioning," in *International workshop on biomedical image registration*, 2006.

[51] C. Weiquing, O. Zongying and S. Weiwei, "A coarse to refined approach of medical image registration based on combining mutual information and shape information," in *International conference on neural networks and brain*, 2005.

[52] R. So and A. Chung, "Non rigid registration by using graph cuts with mutual information," in *IEEE international conference on image processing*, 2010.

[53] G. Gopalakrishnan, S. Kumar, A. Narayanan and M. R., "A fast piecewise deformable method for multi modality image registration," in *Workshop on applied imagery and pattern recognition*, 2005.

[54] A. Vidyarathi and N. Mittal, "A hybrid model for extraction of brain tumor in MR images," in *International conference on signal processing and communications*, 2013.

[55] X. Anping, L. Wang, S. Feng and Q. Yunxia, "Threshold based level set method of image segmentation," in *International conference on intelligent network and intelligent systems*, 2010.

[56] El-fehgi, S. Huang and M. Sid-Ahmed, "X-ray image segmentation using auto adaptive fuzzy index measure," in *Midwest symposium on circuits and systems*, 2004.

[57] A. Tsai, A. J. Yezzi, W. Wells, C. Tempany, D. Tucker, A. Fan, W. Grimson and WillskyAlan, "A shape based approach to the segmentation of medical imagery using level set," in *IEEE transcations on medical imagery*, 2003.

[58] T. Cootes, G. Edwards and C. Taylor, "Active appreance model," in *IEEE transcation on pattern analysis and machine intelligence*, 2001.

[59] J. Weng, A. Singh and M. Chiu, "Learning based ventricle detection from cardiac MR and CT images," in *IEEE transcations medical imagery*, 1997.

[60] N. Duta and M. Sonka, "Segmentation and interpretation of MR brain images: An improved active shape model," in *IEEE transcation on medical imagery*, 1998.

[61] M. Dubuisson and A. Jain, "A modified hausdorff distance for object matching," in *Conference A: Computer vision and image processing*, 1994.

[62] Q. Zhao, J. Kang, H. Tao and W. Hua, "Part based human tracking in a multiple cues fusion framework," in *International conference on pattern recognition*, 2006.

[63] L. Nui, X. Jiang, W. Zhang and S. DongXin, "Image registration based on hausdorff distance," in *International conference on networking and information technology*, 2010.

[64] A. Wang, S. Xiyan, Z. Xiaoxing and H. Wenjuan, "Difference squared hausdorff distance based on medical image registration," in *Chinese control and decision conference*, 2011.

[65] P. Xiaoming, C. Wufan and M. Qian, "Hausdorff distance based non-rigid image registration using feature points," in *International conference on communications, cicuits and systems proceedings*, 2006.

[66] L. Junli, C. Rijuan, J. Linpeng and W. Ping, "A medical image registration method based on weighted mutual information," in *International conference on bioinformatics and biomedical engineering*, 2008.

[67] S. Lixia, Z. Chenping, P. Xiamong and D. Mingyue, "The study on hausdorff distance based image registration methods," in *Chinese journal of image and graphics*, 2003.

[68] Z. Fuqiang, Y. Hongyu, M. Binrong and L. Kucheng, "Image feature based CT-MR image registration," in *Beijing biomedical engineering*, 2000.

[69] B. Zitova and J. Flusser, "Image registration methods: a survey," in *Image and vision computing*, 2003.

[70] D. Gavrila, "A bayesian exemplar based approach to hierarchical shape matching," in *IEEE transcations on pattern analysis and machine intelligence*, 2003.

[71] [Online] Available in http://pixshark.com/tibia-and-fibula-and-femur.htm.

[72] [Online] Available in http://medical-dictionary.thefreedictionary.com/acetabulum.

[73] S. Kirkpatrick, C. Gelatt and M. Vecchi, "Optimization by simulated annealing," *Science magazine,* vol. 220, pp. 671-680, 1983.

Publications by author

- Aseem Vyas, WonSook Lee "Medical image segmentation by transferring ground truth segmentation based upon top down and bottom up approach", *International conference on information technology convergence and series*, Januaury-2015, ISBN : 978-1-921987-21-2
- Aseem Vyas, WonSook Lee " Medical image segmentation by transferring ground truth segmentation" accepted to the *12th international conference on quality control by artificial vision*, 3-5 June 2015, Le creusot, France